IN-SITU AND *OPERANDO* CHARACTERIZATION OF BATTERIES WITH ENERGY-DISPERSIVE SYNCHROTRON X-RAY DIFFRACTION

By

WILLIAM ARTHUR PAXTON

A dissertation submitted to the

Graduate School-New Brunswick

Rutgers, The State University of New Jersey

In partial fulfillment of the requirements

For the degree of

Doctor of Philosophy

Graduate Program in Materials Science and Engineering

Written under the direction of

Thomas Tsakalakos

And approved by

_____

_____

_____

_____

New Brunswick, New Jersey

January 2015

ABSTRACT OF THE DISSERTATION

In-situ and *Operando* Characterization of Batteries with Energy-Dispersive Synchrotron X-ray Diffraction

By **WILLIAM ARTHUR PAXTON**

Dissertation Director:

Thomas Tsakalakos

Batteries play a pivotal role in the low-carbon society that is required to thwart the effects of climate change. Alternative low-carbon energy sources, such as wind and solar, are often intermittent and unreliable. Batteries are able capture their energy and deliver it later when it is needed. The implementation of battery systems in grid-level and transportation sectors is essential for efficient use of alternative energy sources.

Scientists and engineers need better tools to analyze and measure the performance characteristics of batteries. One of the main hindrances in the progress of battery research is

that the constituent electrode materials are inaccessible once an electrochemical cell is constructed. This leaves the researcher with a limited number of available feedback mechanisms to assess the cell's performance, e.g., current, voltage, and impedance. These data are limited in their ability to reveal the more-localized smaller-scale structural mechanisms on which the batteries' performance is so dependent.

Energy-dispersive x-ray diffraction (EDXRD) is one of the few techniques that can internally probe a sealed battery. By analyzing the structural behavior of battery electrodes, one is able to gain insight to the physical properties on which the battery's performance is dependent. In this dissertation, EDXRD with ultrahigh energy synchrotron radiation is used to probe the electrodes of manufactured primary and secondary lithium batteries under *in-situ* and *operando* conditions. The technique is then applied to solve specific challenges facing lithium ion batteries.

Diffraction spectra are collected from within a battery at 40 micrometer resolution. Peak-fitting is used to quantitatively estimate the abundance of lithiated and non-lithiated phases. Through mapping the distribution of phases within, structural changes are linked to the battery's galvanic response. A three-dimensional spatial analysis of lithium iron phosphate batteries suggests that evolution of inhomogeneity is linked to the particle connectivity. Despite a non-linear local response, the average of the measured ensemble behaves linearly. The results suggest that inhomogeneity can be difficult to measure and highlights the power of the EDXRD technique. Additional applications of EDXRD are discussed.

Acknowledgements

Getting a PhD was something that I never originally thought I could do. In retrospect though, embarking on this journey was one of the best decisions I have ever made. While getting a PhD may seem like an individual pursuit, the process requires the contribution of and support by many. In the end, there are many people whom I should acknowledge.

First, I should acknowledge all the great scientists whose names appear in the references sections of this dissertation. Organizing one's work and communicating it in a publication format can be an arduous task and yet it is essential for the progress of science. I am, thus, grateful for all of those who have written before me, making it possible for me to "stand on their shoulders."

Second, I should acknowledge my adviser, Tom Tsakalakos, for his tireless dedication to his students. I consider myself extremely lucky to have had his support from the beginning. I am also extremely grateful for Lisa Klein who has always been available for encouragement and advice throughout the process. Additionally, the advice and support of Glenn Amatucci, Vassilis Keramidas, and K.C. Lim is gratefully acknowledged. My work at Brookhaven wouldn't have been successful without the knowledge of the beamline master Zhong Zhong. Another person whom I attribute to the "Brookhaven-experience" is Koray Akdoğan; I will always think back to the many enlightening discussions we had there.

I have special gratitude for İlyas Şavkliyildiz and Brandon Berke for showing me the ropes in the research group. I owe a lot to the coding mastery of Scott Silver, Wu Yi, Ankur Choksi, and Hui Zhong. Their hard effort has saved me, and other EDXRD researchers, time and frustration. Additionally I would like to thank all the rest of my cohort for making this experience more colorful: Hülya Biçer, Tevfik Ozdemir, Shivani McGee. My graduate experience wouldn't have

been the same without getting to know and working with Bart Visser. Our many discussions about science, life, and nature will always be remembered.

Certainly, I owe so much to my family for supporting me along the path of life: my parents, Helen and Art Paxton; my sisters, Emma and Daria Paxton; my grandparents, Mary and David Sive, Dorothy and Norman Paxton. Lastly, I thank all my friends, old and new, who make my life all the much richer.

Table of Contents

List of Figures

List of Tables

1. Introduction

1.1 Motivation

As the world population continues to grow beyond 7 billion, the demand for energy grows as well. Fossil fuels have supplied most of humanity's energy up to the present but they are finite and will eventually diminish. The combustion of fossil fuels also carries a large environmental cost by accelerating climate change and negatively impacting the areas where they are developed and used. The need for renewable and clean energy sources is paramount for sustaining future generations. Recently, much progress has been made in the development and implementation of renewable energy technologies such as wind turbines, geothermal and photovoltaics. Still, these technologies are costly, noncompetitive, and are only as effective as our ability to store the energy that is generated from them.

Not only are clean and renewable energy sources needed but safe and efficient methods of energy storage are equally as important. For energy generated from wind and solar, there is a large time mismatch between supply and demand. When the sun is shining, there is available solar energy but the demand for lighting is usually when the sun has already set. In the case of wind, the energy generated from wind is highly dependent on weather patterns and often times the electrical grid isn't capable of managing those large fluctuations of power. When energy from wind and solar is stored in an energy storage device, then these sources are better able to replace applications where fossil fuels dominate.

Batteries are one of the most important energy storage devices. A battery consists of at least one electrochemical cell where these cells, simply put, are portable chemical-reaction chambers. Cells provide a supply of electrons by way of an electrochemical reaction and are comprised of two electrodes, positive and negative, a separator, and electrolyte. The

performance characteristics of a cell are dependent on the selection of materials used to build them.

Lithium ion batteries play an important role in today's society. In a lithium-ion cell, lithium ions travel from one electrode to another and create a usable electrical current. During this process, the electrode materials accommodate lithium ions in to a host structure by a process known as intercalation. Since lithium ion batteries (LIB) were commercialized in 1991 by Sony Corporation, the technology has enabled high energy density batteries at low costs enabling a portable electronics revolution. In 2010, 67% of the population owned a mobile phone. [1] Today, even more people around the world rely on LIBs to power their cell phones, laptops and other portable electronic devices. Recently, engineers are starting to use LIBs in vehicles, power tools, and other larger devices. However, as ubiquitous as LIBs have become they still aren't without issues. LIBs have limited lifetimes, performance characteristics, and safety issues. [2]

Much theory and experimentation has gone in to the development of LIBs, enabling better electrode materials, processing and construction methods, but there are still many challenges that lie ahead. One main hindrance in the development of better batteries is that once a battery is manufactured the reaction that is taking place is hidden and buried. Traditionally, the only feedback mechanism to a cells performance is the voltage between its two terminals. Methods such as impedance spectroscopy have allowed more information to be collected from cells but impedance and current-voltage curves are still only measurements of the entire battery or cell. [3] These methods are limited in their ability to measure smaller-scale mechanisms on which the batteries' performance is so dependent.

The limitations of traditional characterization techniques require engineers and scientists to develop better tools and methods for understanding how these materials behave in battery

systems. Recently, much progress has been made in the area of in-situ diffraction; that is to collect diffraction patterns while a battery or reaction is in action. For lithium-insertion battery chemistry such as lithium iron phosphate, scientists have done in situ experiments by building specialized reaction chambers and forcing the reaction. In other cases special one-use batteries are made where the packaging contains a Beryllium window for x-rays to penetrate. While the data collected from these experiments are useful, they still fail to reveal the entire picture. Most of the time, the design of the batteries, cells, or reaction chambers are far from their natural design under normal operation. Furthermore, the size and resulting capacity of these specially designed cells are far from what will be manufactured and sold for everyday use.

There is a large disconnect between the research characterization methods for batteries in the laboratory from what is manufactured for everyday use. Batteries created in the laboratory for studies are usually built with geometry specific to the study that is being performed. Also, they are usually very small in capacity and are able to be cycled quickly with low current. For batteries designed for everyday use, their geometry is determined by the most efficient manufacturing process and their capacities can be multiple orders of magnitude larger. These major differences create a challenging gap for the scientists developing new batteries and the engineers manufacturing them for real-world applications.

1.2 Literature Review

In battery research, *in-situ* experimentation has proven to be a valuable method for understanding underlying reaction mechanisms. The Latin term *in situ* literally translates to “in position” and, in the context of electrochemistry, refers to an experiment which is performed while the electrochemical reaction is taking place. Diffraction using X-rays, and sometimes neutrons, has been a preferred method for in-situ experimentation because of its ability to

provide data on structural changes as they occur. *In-situ* diffraction experiments on batteries date back as far as 1992 and continue to advance the field of battery research today. [4-11]

Proudly, some of the first in-situ diffraction experiments on lithium ion batteries were carried out by Rutgers research faculty in 1996. Then, Glenn Amatucci, Jean-Marie Tarascon, and Lisa Klein were able to isolate, for the first time, a new phase in the Li_xCoO_2 solid solution by constructing a cell that would allow for the penetration of X-rays. [6] Later, in 2002, M. Morcrette, along with others, published the details of their cell which used Bellcore's plastic laminate electrodes. With their cell, they were able to screen new materials including different phosphate-based electrodes. Further advances in low-Z packaging materials and instrumentation, mainly synchrotron radiation, have allowed for a stronger understanding of the structural evolution of electrode materials. [9]

Recently, much lithium battery research has focused on the lithium iron phosphate (LFP) material for use as a positive electrode material in rechargeable lithium-ion batteries. This cathode material is of great interest due to its advantages over now-ubiquitous cobalt oxide materials which include low raw-materials cost, environmental friendliness, long cycle lifetime, and thermal stability. [12,13] Such characteristics make it the most desirable cathode material for use in electric and hybrid-electric vehicle applications. There have been quite a few in-situ diffraction studies on the LFP. Ho Chul Shin *et al.* studied Cr doping in carbon coated lithium iron phosphate cells using both conventional and synchrotron x-ray diffraction. Shin's cells were specially designed for in-situ experimentation using a hole for x-ray transmission and Kapton windows. [10] Xiao-Jian Wang *et al.*, in order to study the delithiation of lithium iron phosphate, configured a in-situ XRD chemical reaction chamber and forced the delithiation process chemically. Their study used angular synchrotron x-ray diffraction covering a range of about 15° collecting diffraction patterns every minute. [7,8]

Energy dispersive x-ray diffraction is well suited for *in-situ* experimentation due to its inherent fast collection time compared to angular dispersive x-ray diffraction. [14] In fact, some of the earliest experiments, dating back to the early 70s, were *in-situ* high-pressure studies. [15] Interestingly enough, EDXRD was used to study the chemical intercalation of lithium salts in Gibbsite in 1999 but not until 2010 was EDXRD used to study any electrochemical process. Rijssenbeek *et al.* were able to measure the reacting phases as a function of charge and discharge cycles in prototype sodium metal-halide cells. [16] Using EDXRD they were able to achieve both space and time resolved diffraction patterns. With their data they were able to show a reaction front within the cell moving from one electrode to the other. To their great advantage, their experiment revealed intermediate phases which were negatively affecting the cell's performance.

1.3 Scope of Work

Scientists and engineers need better tools to analyze and measure the performance characteristics of "product-type" manufactured batteries. Energy-dispersive x-ray diffraction offers unique capabilities to probe batteries *in situ* and *operando* conditions. This dissertation explores the potential of using energy-dispersive x-ray diffraction to probe commercial lithium ion batteries. It then applies the technique to solve specific challenges facing lithium ion batteries.

Chapter two contains a technical background and justification of why EDXRD could be applied to lithium ion batteries. Chapter three, based on a paper published in the Journal of Power Sources, addresses the use of EDXRD in tracking inhomogeneity in high-capacity lithium iron phosphate batteries. Chapter four, based on a paper published in the Journal of Materials Research, extends the work of chapter three by studying the Asynchronous stoichiometric response in lithium iron phosphate batteries. Chapter five covers unpublished data collected

from batteries including lithium carbon monoflouride, lithium manganese oxide, and lithium iron phosphate. Chapter six includes a summary and future work. Additionally, appendix A describes different computer-based tools that are used in the data analysis process. Lastly, Appendix B includes a paper which describes an EDXRD study, outside of the context of batteries, on the anisotropic thermal expansion of zirconium diboride.

1.4 References

[1] S. Fletcher, Bottled Lightning: Superbatteries, Electric Cars, and the New Lithium Economy. Hill and Wang, (2011)

[2] J. Mouawad and C. Drew, Boeings battery problems cast doubt on appraisal of new technologies, The New York Times, Jan. (2013)

[3] M. Salomon, Lithium-Ion Batteries, ch. 2. McGraw Hill, 4 (2002).

[4] A. M. Fogg and D. O'Hare, 11 (1999) 1771-1775.

[5] J. N. Reimers and J. R. Dahn, Journal of The Electrochemical Society, 139 (1992) 2091-2097.

[6] G. G. Amatucci, J. M. Tarascon, and L. C. Klein, Journal of The Electrochemical Society, 143 (1996) 1114-1123.

[7] X.-J. Wang, H.-Y. Chen, X. Yu, L. Wu, K.-W. Nam, J. Bai, H. Li, X. Huang, and X.-Q. Yang, Chem. Commun., 47 (2011) 7170-7172.

[8] X.-J. Wang, C. Jaye, K.-W. Nam, B. Zhang, H.-Y. Chen, J. Bai, H. Li, X. Huang, D. A. Fischer, and X.-Q. Yan,, J. Mater. Chem., 21 (2011) 11406-11411

[9] M. Morcrette, Y. Chabre, G. Vaughan, G. Amatucci, J.-B. Leriche, S. Patoux, C. Masquelier, and J.-M. Tarascon, Electrochimica Acta, 47 (2002) 3137- 3149.

[10] H. C. Shin, S. B. Park, H. Jang, K. Y. Chung, W. I. Cho, C. S. Kim, and B. W. Cho, Electrochimica Acta, 53 (2008) 7946 - 7951.

[11] M. A. Rodriguez, D. Ingersoll, S. C. Vogel, and D. J. Williams, Electrochemical and Solid-State Letters, 7 (2004) A8-A10.

[12] A. K. Padhi, K. S. Nanjundaswamy, and J. B. Goodenough, Journal of The Electrochemical Society, 144 (1997) 1188-1194.

[13] S.-Y. Chung, J. T. Bloking, and Y.-M. Chiang, Nature Materials, 1 (2002) 123-128.

[14] B. K□ampfe, F. Luczak, and B. Michel, Particle & Particle Systems Characterization, 22 (2005) 391-396.

[15] E. Laine and I. Lhteenmki, Journal of Materials Science, 15 (1980) 269-277.

[16] J. Rijssenbeek, Y. Gao, Z. Zhong, M. Croft, N. Jisrawi, A. Ignatov, and T. Tsakalakos, Journal of Power Sources, 196 (2011) 2332 - 2339

[17] M. Itagaki, N. Kobari, S. Yotsuda, K. Watanabe, S. Kinoshita, and M. Ue, Journal of Power Sources, 135 (2004) 255 - 261.

2. Technical Background

2.1 Lithium-Ion Batteries

A lithium ion battery is an energy storage device which relies on the high chemical potential of lithium. In a typical intercalation lithium ion battery, lithium ions are transferred between host electrodes in a reversible fashion. A schematic of a typical commercial lithium ion battery is given in Figure 2.1. The positive electrode, also known as cathode, is a lithium oxide powder that is deposited on a foil, typically made of aluminum. During discharge, the positive electrode is the site of the reduction process. Conversely, the negative electrode, also known as the anode, is the site of oxidation process. A typical anode is composed of carbon and deposited on a copper foil. Between the anode and cathode is a micro-porous separator material and a non-aqueous electrolyte. The role of the separator is to promote ionic transport while simultaneously preventing electronic transport. The electrolyte serves as a conductive medium for both.

When the foils, more commonly referred to as current collectors, are connected through an external resistive circuit, the electrochemical discharge process begins. Lithium ions diffuse through the electrolyte and separator over to the cathode side. The associated electron in the anode flows through the circuit to the cathode where it is used to maintain charge balance with the lithium ion. When an external voltage is applied to the current collectors, the lithium ion battery will charge. This process is essentially opposite to the discharge process. The cathode is undergoes an oxidation reaction and the lithium travels back to the anode. [1]

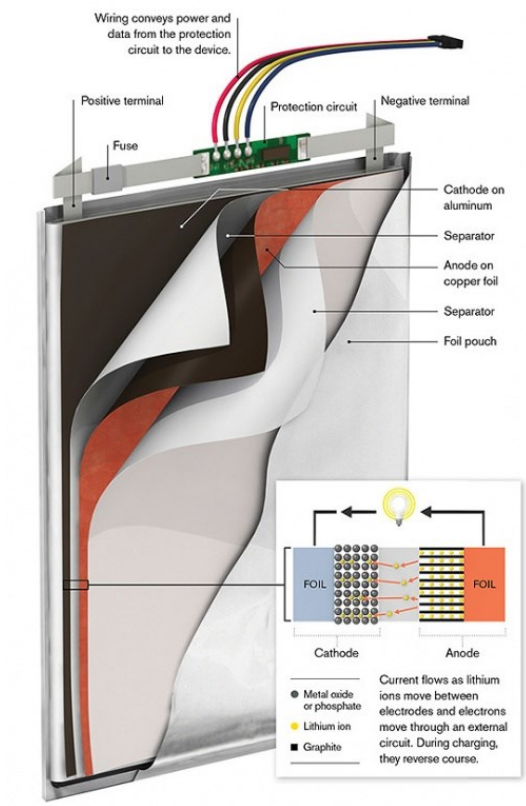

Figure 2.1 Schematic of a typical lithium ion battery [2]

The following are the typical cathode, anode, and full reactions for a lithium ion battery

$Li_{1-x}MO + xLi + xe^- \rightarrow LiMO$ (cathode reduction reaction)

$LiC \rightarrow xLi + xC + e^-$ (anode oxidation reaction)

$LiC + MO \leftrightarrow C + LiMO$ (reversible redox reaction)

where MO is a metal oxide material. The cathode metal oxide material is commonly a cobalt or cobalt-alloy oxide. Other common cathode materials are iron phosphate or manganese oxide, which are chosen for their electrochemical characteristics.

2.2 Diffraction Background

In a solid material, one where atoms are arranged in a three dimensional periodic array, a crystal lattice is formed. The smallest divisible repeating unit in a crystal lattice is defined as a unit cell. When the lattice extends beyond approximately 10 unit cells in any one direction, a scattering phenomenon known as diffraction can occur.

When considering an x-ray photon incident on an ideal crystal, the photon scattering event is perfectly elastic. Thus, from the law of conservation of energy, the magnitude of the wave vectors should be equal:

$$|\boldsymbol{k}_i| = |\boldsymbol{k}_s| = \frac{2\pi}{\lambda}$$

where $\boldsymbol{k}_i$ is the incident wave and $\boldsymbol{k}_s$ is the scattered wave and λ is the wavelength.

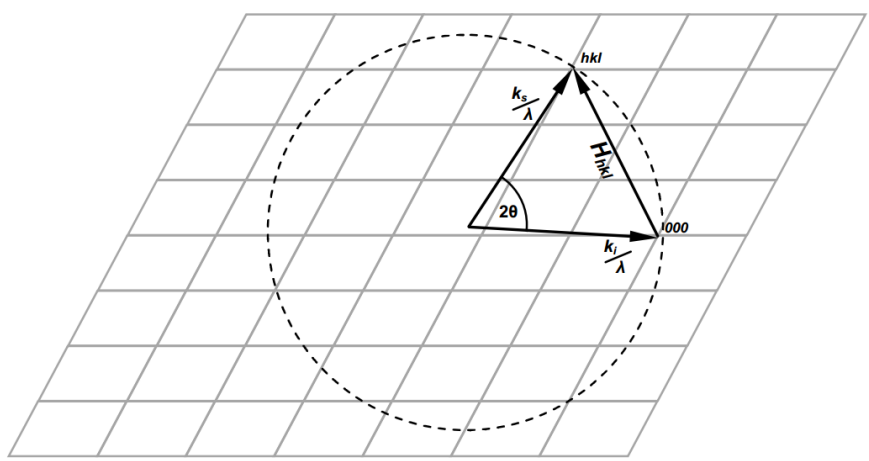

Figure 2.2 Two-dimensional representation of Ewald's Sphere

Two-dimensional representation of the sphere of reflection in the reciprocal lattice. Here the conservation of momentum is satisfied for any set of planes whose point *hkl* falls on the surface of the sphere [3]

The scattering event is caused by an interaction between the photon and the negative charge from electrons in the lattice. For diffraction, it is convenient to consider the charge density of the lattice. We can now consider the scattering event as an interaction between the incident wave and a static plane wave of the electron density. Given the law of conservation of momentum, the momentum transfer from the incident wave to the lattice, $\boldsymbol{q}$ is given as:

$$\boldsymbol{q} = \boldsymbol{k}_s - \boldsymbol{k}_i = 2\pi\boldsymbol{H}$$

where $2\pi\boldsymbol{H}$ is the reciprocal lattice vector. [4] Combining the two prior equations one obtains

$$\frac{\boldsymbol{k}_s - \boldsymbol{k}_i}{\lambda} = \boldsymbol{H}_{hkl}$$

providing a relationship between the incident, scattered, and lattice vectors and the wavelength. Here, the lattice vector is given subscripts hkl to notate the miller index by which the diffraction event is occurring. Figure 2.2 provides a graphical, two-dimensional representation in reciprocal space of the geometrical condition for diffraction. [3]

Figure 2.3 shows the geometrical condition for diffraction in real space. Here, the equation is rearranged in to the commonly known Bragg's Law:

$$n\lambda = 2d_{hkl}\sin\theta$$

where n is integer number of atomic planes, λ is wavelength of incident beam, d_{hkl} is inter-planar spacing and θ is the angle between the incident beam and the atomic plane. [5]

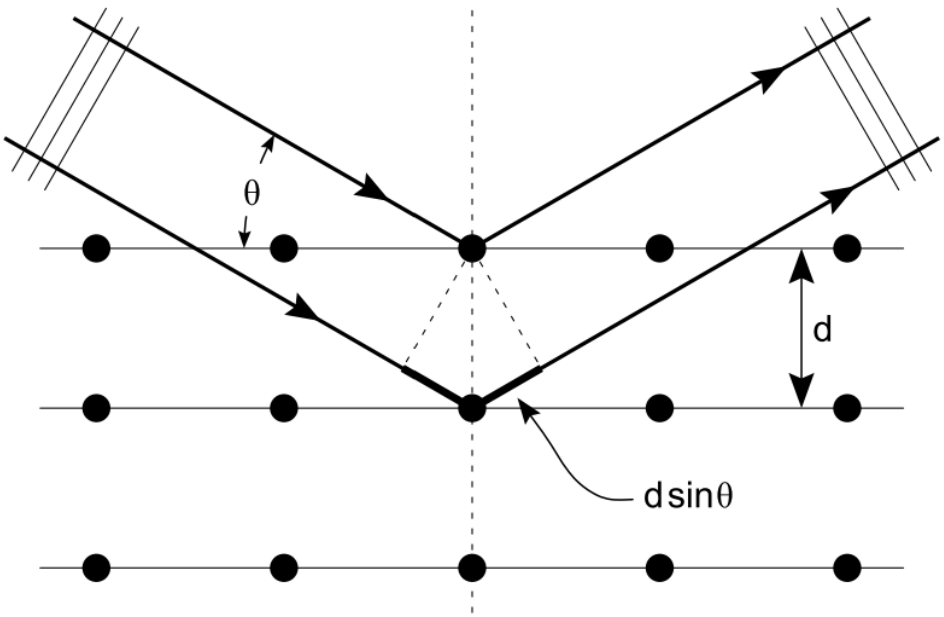

Figure 2.3 Bragg diffraction from a cubic crystal lattice

Bragg diffraction from a cubic crystal lattice where plane waves incident on a crystal lattice at angle are partially reflected by successive parallel crystal planes of spacing. The superposed reflected waves interfere constructively if the Bragg condition is satisfied. [6]

2.3 Synchrotron Radiation

In recent years, x-ray techniques have benefited from the production of facilities that create synchrotron radiation. Synchrotron radiation is created when charged particles, usually electrons or protons, are accelerated to almost the speed of light. As the charged particles are rapidly accelerated, a large amount of energy is released in the form of photons and ranging across a wide portion of the electromagnetic spectrum. The facilities are usually built in structure of a ring where there are many end-stations for experimentation using different filters, monochromators, or focusing optics.

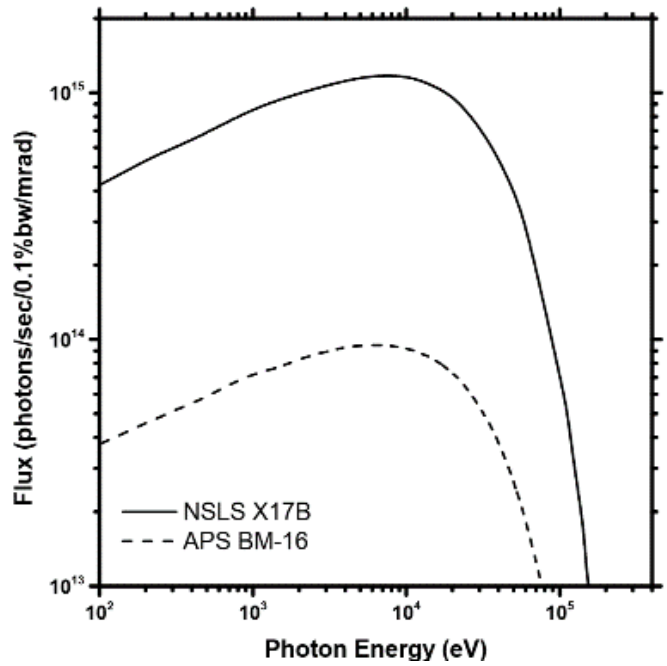

Figure 2.4 Sample synchrotron spectra

The photon energy spectrum of beamline X17B1 at National Synchrotron Light Source at Brookhaven National Laboratory where the wide range of energies (up to 200 keV) with very high intensity was used for this study. A comparison with a similar beam line at Advanced Photon Source at Argonne National Laboratory is provided.

As previously mentioned, the development of synchrotron facilities has been a boon for analytical x-ray techniques. Synchrotron radiation covers a large range of energies and that allows for superior data acquisition. In the case of EDXRD, it enables the ability to probe many different crystallographic planes at the same time, resulting in fast and rich data acquisition. The X17B1 beam line at NSLS delivers photons with energies up to 200 keV by the use of a super-conducting wiggler. [7] The use of high-energy, sometimes referred to as hard, x-rays is advantageous because the x-rays aren't absorbed well in a solid material and therefore allow for deep penetration. These properties of synchrotron radiation, coupled with overall high intensities, allow for rich data collection and experimentation that was previously not possible.

2.4 Energy-Dispersive X-ray Diffraction

Energy dispersive x-ray diffraction (EDXRD) is an x-ray scattering technique that uses polychromatic radiation at a fixed diffraction angle to satisfy the Bragg condition. For a quantitative understanding of EDXRD, let us first consider the Einstien-Planck Equation

$$E = \frac{h}{\nu}$$

where E is the energy of a photon, h is Planck's constant and ν is the frequency. The frequency can also be represented as

$$\nu = \frac{c}{\lambda}$$

where c is the speed of light and λ is the wavelength of the photon. Combining the two prior equations we obtain

$$E = \frac{hc}{\lambda}$$

which gives a convenient definition of the energy, E. Remembering Bragg's Law

$$n\lambda = 2d \sin\theta$$

and combining with we obtain,

$$E = \frac{\frac{1}{2}hc}{d \sin\theta}$$

and by recognizing that $\frac{1}{2}hc = 6.199 \text{ keV} \cdot \text{Å}$, we are left with

$$E_{hkl} \text{ (keV)} = \frac{6.199}{\sin\theta \, d_{hkl}(\text{Å})}$$

which is the governing equation of EDXRD. Here, E_{hkl} is the energy of the scattered photons from lattice plane (*hkl*), measured in keV, and d_{hkl} is the spacing of the atomic plane with the Miller index (*hkl*), measured in Angstroms. It is important to note that the measured quantity $\frac{1}{d_{hkl}}$ is equivalent to the magnitude of the reciprocal lattice vector, $|\boldsymbol{H}_{hkl}|$. Because the diffraction angle θ is fixed, the $\frac{6.199}{\sin\theta}$ term is constant thus allowing EDXRD to measure $|\boldsymbol{H}_{hkl}|$ directly and with great precision.

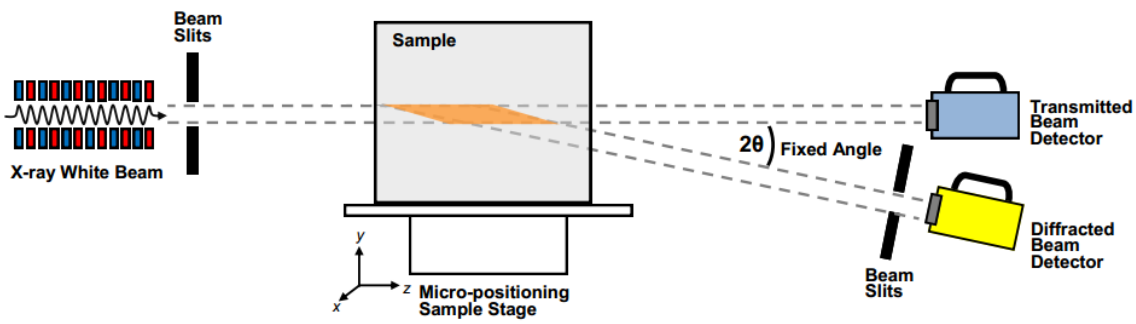

Figure 2.5 Schematic of the EDXRD apparatus used at the NSLS beamline X17B1

Schematic of the EDXRD apparatus used at the NSLS beamline X17B1 where a white x-ray beam is generated using a super-conducting wiggler and shone into a sample as shown. The sample is manipulated on a micro-positioning sample stage and the diffracted beam is recorded at a fixed angle 2θ

Figure 2.5 is an illustration of the EDXRD apparatus at the National Synchrotron Light Source beamline X17B1 where synchrotron radiation is utilized to supply photons with energies up to 200 keV. The broad-bandwidth white' x-ray beam passes through tantalum collimating slits before it reaches a stationary sample. By using the Laue transmission method, the diffracted x-rays pass through additional collimating slits and are then collected with a germanium detector positioned at a fixed angle, 2θ.

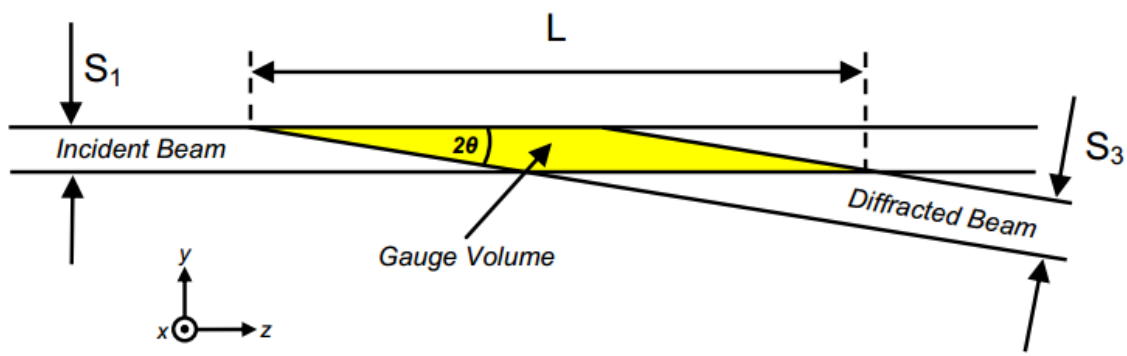

Figure 2.6 Geometry of gauge volume

The volume probed in an EDXRD experiment is referred to as the gauge volume (GV). The dimensions of the gauge volume are determined by the beam slits shown in Figure 2.6. The gauge volume is the shape of a parallelepiped where the height and width are determined by the incident beam slits. The length of the GV is determined geometrically by the following formula

$$L = \frac{S_1}{\sin 2\theta} + \frac{S_3}{\tan 2\theta}$$

where S_1 and $S_3$are the slit openings in the x-y plane perpendicular to the z-axis. [7]

Diffracted x-rays are measured using a cryogenically cooled Germanium detector. The detector stores the number of photon counts in to a multi-channel analyzer with 8192 independent channels. For calibration, a relationship between channel number, energy, and interplanar spacing is determined using a set of known standards where the x-ray florescence and diffraction peaks of each are used in the calibration.

2.5 The Application to Lithium-Ion Batteries

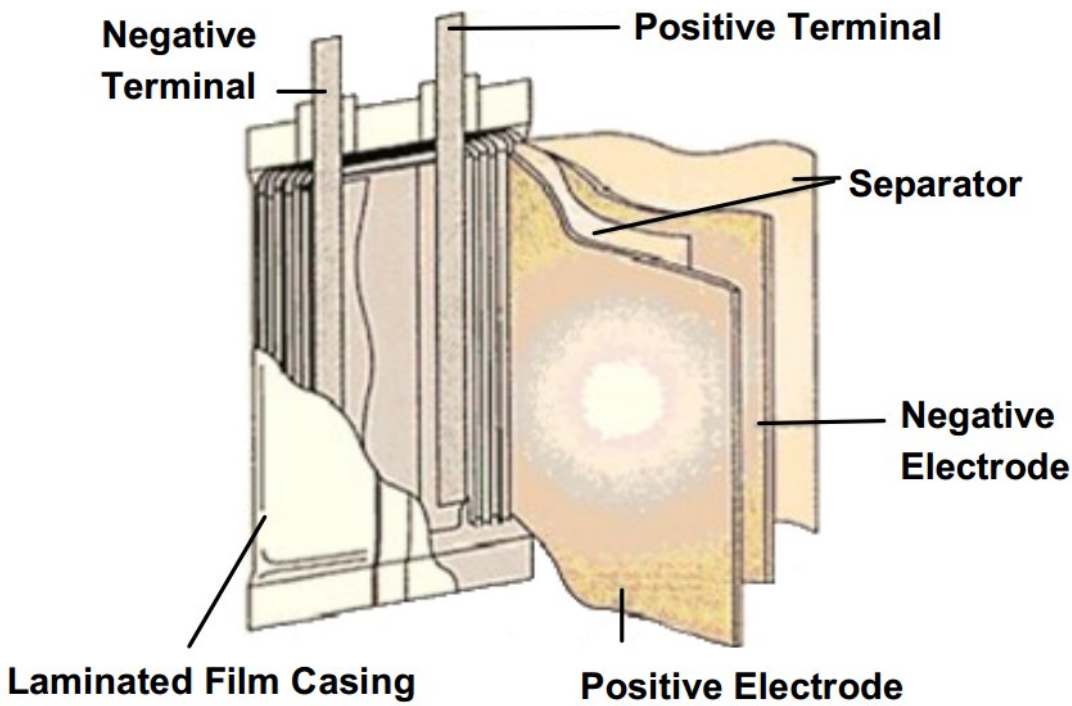

Figure 2.7 Typical construction of a lithium-ion polymer cell [7]

When using EDXRD to measure lithium ion batteries, it is important first consider the mechanisms by which they are constructed. The mechanical construction of a typical lithium-ion polymer cell is shown in Figure 2.7. Here, each lithium-ion cell consists of a positive electrode, separator, positive electrode, and electrolyte. The cell is constructed by a tape casting process where the electrode powders are deposited on to current collectors and separators. The next step is a stacking of all functional layers, a spiral winding process, and then a pressing step to flatten the layers. [9] Once completed, what is left is a multi-layer electrochemical structure housed in an aluminized polymer pouch filled with a non-aqueous electrolyte.

In order to isolate the gauge volume solely in a single region of the cell to get a clearly resolved signal, the cell should be transversely mounted in the beamline. Figure 2.8 shows how the cell is oriented with respect to the incident and diffracted beam where $\vec{n}$ represents the diffraction vector in real space.

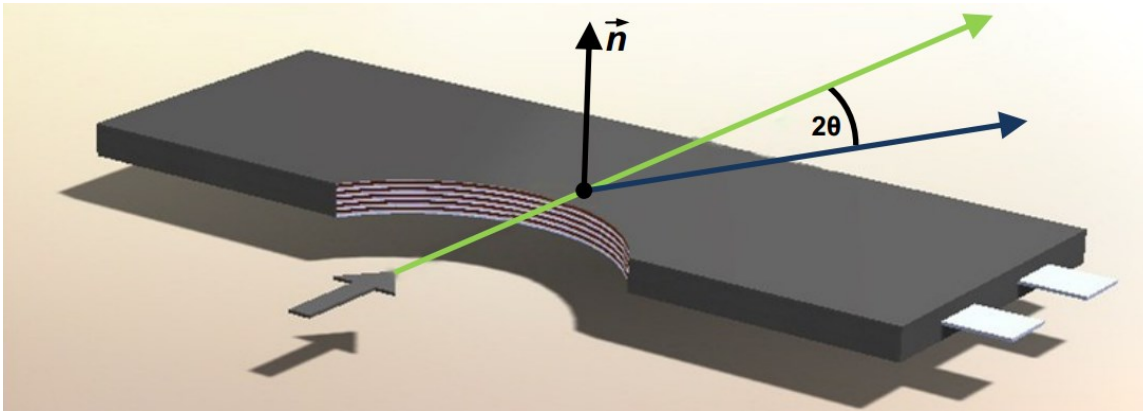

Figure 2.8 Orientation of diffraction vectors

Simulation showing orientation of diffraction vectors in relation to the lithium-ion battery. A cutaway of the battery is shown to reveal layer structure. Layers not to scale.

The transverse mounting of the cell is an important aspect for a number of reasons. First, it allows for the gauge volume to sit solely in a single component of the cell, such as the positive or negative electrode, allowing for a clear diffraction signal. This is achieved by the reducing the S_1 slit dimension to a small value. Then, the planar structure of the cell allows one to increase the width of the gauge volume to have a favorable signal to noise ratio. What is left is a GV that is of a flat planar geometry. This allows for excellent intra-layer resolution and reasonable topological resolution.

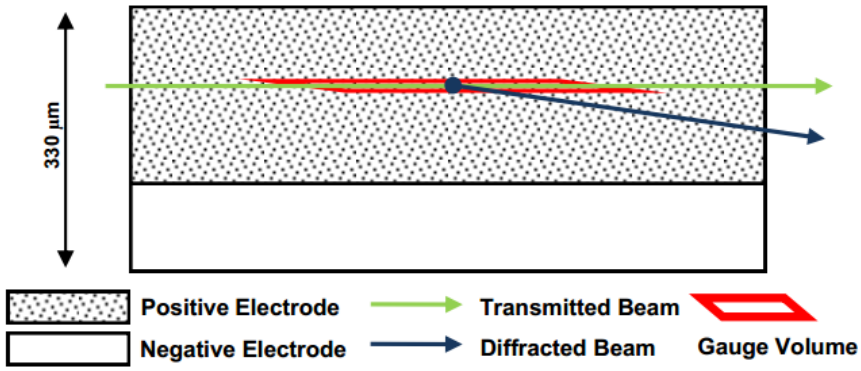

Figure 2.9 Gauge volume positioning within electrode layers

The use of a battery controller, or cycler, is also important for such EDXRD experiments. In the experiments described in this thesis, and Arbin model BT2000 was used. The lead wires were run in to the experimental hutch and clamped on to the battery terminals as shown in Figure

2.6 Data Collection

There are three categories of data that can be collected in an EDXRD experiment. First is a tomographic scan, where the total number of all scattered photons is plotted as a function of position. Second, one can consider the diffraction spectra, itself, which contains crystallographic information and is primarily used for phase and strain analysis. Lastly, by fitting a profile shape function to specific reflection peaks, one can obtain information on defects within the diffracting crystals as well as the size of the reflecting domain. Each category, as it pertains to lithium ion batteries, will be covered below.

2.6.1 Tomographic Profile

A tomographic profile is obtained when one just considers the total scattered intensity of photons. Since the incident photon beam contains a white spectrum, data is collected for all

diffraction energies, allowing for very short collection times (one second). The advantage is that as the beam passes through different phases, the intensity of the beam changes as well. As a result, it is a very effective way to quickly probe the internal structure of a cell. One can measure with good accuracy the spacing and repetition of the layers and thereby use EDXRD as a quick analysis for quality control and failure analysis.

2.6.2 Diffraction Spectra

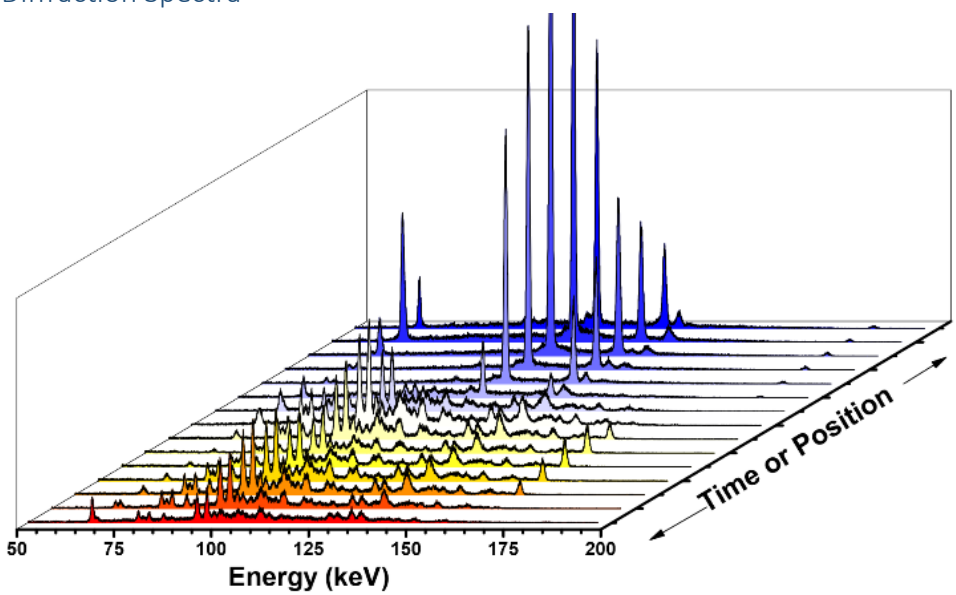

Figure 2.10 Sample data from an EDXRD experiment

Sample data from an EDXRD experiment where the x-axis is Energy and y axis is number of photon counts. In this figure multiple spectra are shown in a waterfall pattern. Because collection time is very short for EDXRD, multiple spectra are usually collected and are often a function of time or position.

The diffraction spectra collected from an EDXRD experiment contain a lot of useful information. From the diffraction spectra one can retrieve crystallographic structural information from each phase present within the diffraction volume. This is because a broad range of energies are collected, and consequently, a wide range of Bragg reflections are observed. Furthermore, collection time for a typical spectra is about 1-2 minutes. Because of the short time, it is easy to look at many diffraction spectra as a function of time, position, or

other variables. Figure 2.10 shows sample spectra as a function of position in a battery. After each spectra was collected the specimen was moved such that the gauge volume was shifted roughly 40 micrometers. Here you can see the changes in phases are quite distinct, providing spatial phase mapping. This ability to provide structural-crystallographic data from within a sample is the reason why EDXRD is powerful as a true *in-situ* measurement.

2.6.3 Peak Shape Analysis

Additional information can be extracted from the diffraction spectra by fitting a peak shape formula to each peak. The process first involves isolating a peak, or set of peaks, from a spectrum, removing the background, and fitting an analytical function using a least-squares method. The most common functions are Gaussian, Lorentzian, or Pseudo-Voigt which is a convolution of the Gaussian and Lorentzian formulas. The advantage of using a quantitative peak shape analysis is that we can get accurate values for the center, height, area, and width (FWHM) for each peak. This is especially useful when peaks are overlapping and convoluted. In this study computer software was used to automate these quantitative peak fitting process. [10]

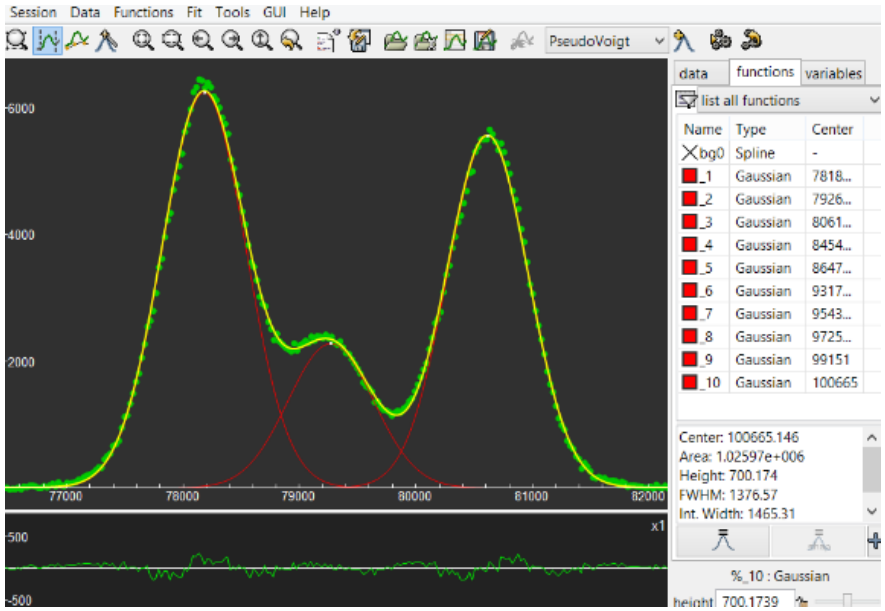

Figure 2.11 Screenshot from peak-fitting software fityk

The full-width-half-maximum (FWHM) of each peak is of particular importance because the broadening of a diffraction peak is generally caused by a small crystallite size, strains, and faulting. However, there is also another contributor to peak broadening which is the instrumentation itself. This must be measured and accounted for before considering any real broadening effects. The equation below shows the relationship between observed (β_o), instrumental (β_i), and real (β_r) broadening when using a Guassian profile shape function.

$$\beta_o{}^2 = \beta_i{}^2 - \beta_r{}^2$$

The quantity, is measured using a lanthanum hexaboride (LaB_6) standard provided by National Institute of Standards. The powder standard is engineered to show no ``real'' broadening effects. As a result, the FWHM of the LaB_6 peaks are used to determine the instrumental broadening as a function of energy.

The real broadening, β_r, is then determined for a set of reflections and its squared-value is plotted. A line can be fit and using the equation below, and the size and strain contributions can be separated. This equation is

$$[\beta_r(E)]^2 = \left(\frac{K\left(\frac{1}{2}hc\right)}{L\sin\theta}\right)^2 + (2\epsilon E)^2$$

where $\beta_r(E)$is the real broadening in energy, K is the Scherrer constant, h is Planck's constant, c is the speed of light, L is the size of the coherent reflecting domain, θ is the diffraction angle, ϵ is the strain, or variation in d-spacing and E is the energy.[11]

From the line profile analysis described above, one can measure the coherent-reflecting domain size and average micro-strain within. Coupled with the spatial and temporal resolution of the EDXRD technique, this information can be used to study phase transformation processes.

2.7 References

[1] T.B. Reddy, Linden's Handbook of Batteries, Fourth Edition, McGraw Hill, (2002)

[2] K. Bullis, Lithium-Ion Batteries, MIT Technology Review, (2012).

[3] B. E. Warren, X-ray Diffraction. Courier Dover Publications, (1969).

[4] Khachaturian, Theory of structural transformations in solids. John Wiley and Sons, New York, NY, (1983).

[5] Krawitz, Introduction to diffraction in materials, science, and engineering. New York: John Wiley,(2001).

[6] Wikipedia, X-ray crystallography — Wikipedia, the free encyclopedia, (2013).

[7] W. Thomlinson, D. Chapman, N. Gm¨ur, and N. Lazarz, Nuclear Instruments and Methods in Physics Research Section A: Accelerators, Spectrometers, Detectors and Associated Equipment, 266 (1988) 226–233.

[8] B. Berke, PhD thesis, Rutgers, The State University of New Jersey, (2012).

[9] W. C. Ltd., Electropaedia - cell mechanical construction, (2013).

[10] J. Dahn and G. M. Ehrlich, Lithium-Ion Batteries, ch. 26. McGraw Hill, 4 (2002).

[11] M. Wojdyr, Journal of Applied Crystallography, 43 (2010) 1126–1128.

[12] L. Gerward, S. Mørup, and H. Topsøe, Journal of Applied Physics, 47 (1976) 822–825.

3. Tracking inhomogeneity in high-capacity lithium iron phosphate batteries

3.1 Preface

This chapter is based on a manuscript published in the Journal of Power Sources (J. Power Sources, 275 (2015) 429-434). The full list of authors includes William A. Paxton, Zhong Zhong, and Thomas Tsakalakos. The role of William A. Paxton was to design and perform all experiments, process and analyze all data, and prepare the manuscript for submission.

3.2 Graphical Abstract

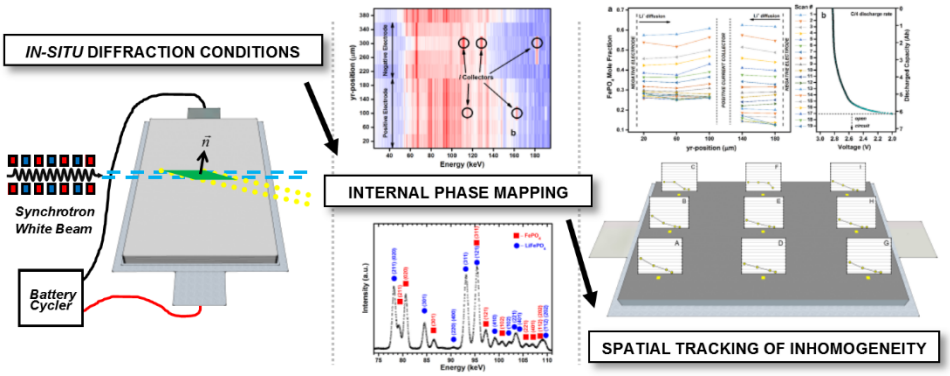

3.3 Highlights

- *In-situ* and *operando* profiling of a real-world 8 Ah lithium iron phosphate cell is carried out at NSLS X17-B1
- Spatial tracking of inhomogeneity in three dimensions is achieved while discharging
- A strong correlation between inhomogeneity evolution and cell overpotential is observed
- Results follow resistive-reactant model where particles sequentially contribute in order of their inter- and intra-particle connectivity

3.4 Abstract

Energy-dispersive x-ray diffraction (EDXRD) is one of the few techniques that can internally probe a sealed battery under operating conditions. In this paper, we use EDXRD with ultrahigh energy synchrotron radiation to track inhomogeneity in a cycled high-capacity lithium iron phosphate ($LiFePO_4$) cell under *in-situ* and *operando* conditions. A sequence of depth-profile x-ray diffraction spectra are collected with 40 micrometer resolution as the cell is discharged. Additionally, nine different locations of the cell are tracked independently throughout a second discharge process. In each case, a two-peak reference intensity ratio analysis (RIR) was used on the $LiFePO_4$ (311) and the $FePO_4$ (020) reflections to estimate the relative phase abundance of the lithiated and non-lithiated phases. The data provide a first-time look at the dynamics of electrochemical inhomogeneity in a large, product-type battery manufactured for electric vehicle applications. We observe a strong correlation between inhomogeneity and overpotential in the galvanic response of the cell. Additionally, the data closely follow the behavior that is predicted by the resistive-reactant model originally proposed by Thomas-Alyea. Despite a non-linear response in the independently measured locations, the behavior of the ensemble is strikingly linear. This suggests that inhomogeneity, although very important to the battery's performance and cycle life, can be difficult to observe with macroscopic measurements and highlights the power of the EDXRD technique.

3.5 Introduction

The commercial introduction of lithium-ion batteries has enabled a worldwide portable-electronics revolution. More recently they are being used for much larger portable devices: hybrid gaselectric and all-electric vehicles. Lithium-ion batteries offer competitive properties (i.e. energy density, cycle life, and low self-discharge rates) which have proved advantageous for

the development of portable electronics.[1] However, for successful implementation in electric vehicle applications the current technological state of lithium-ion batteries needs improvement. Specifically, fire susceptibility and limited driving ranges of electric vehicles are pushing researchers and engineers to improve the durability, safety, and energy density of lithium-ion batteries.[2]

Lithium iron phosphate ($LiFePO_4$) is an electrode material which offers a high cycle life, excellent thermal stability, and is composed of relatively earth abundant materials.[3] For these reasons, it is welcomed as the next-generation lithium-ion battery for electric vehicles. Structurally, $FePO_6$ octahedra combine with PO_4 tetrahedra to form a crystalline framework which can accommodate lithium intercalation. While the exact nature of lithium intercalation remains elusive, it is generally known that lithium diffusion is one-dimensional and the transformation is biphasic, evident in its flat voltage profile. [3]

Following its discovery by Padhi *et al.* 1997, lithium iron phosphate was regarded as a low-power material due to its poor intrinsic electronic and ionic conductivity.[4] Recently however, researchers have found that high-rate performance is possible with a reduction of the particle size and modification of the surface chemistry.[5,6] Synthesizing nano-sized particles can reduce the bulk diffusion distances and adding a conductive surface coating improves intra-particle conductivity. With high-rate capability now achievable, lithium iron phosphate is a prime contender for use in electric vehicle batteries. However, because its theoretical energy density is 30% less than well-established oxide electrodes (NCA) its adoption remains a formidable challenge

For electric vehicles, theoretical energy density is still only one factor which influences driving range. A more important indicator of predicting and achieving a desirable long driving

range would be the effective energy density of an entire battery pack. One strategy to improve effective energy density is to scale up the capacity of the electrochemical cell from which a battery is composed. By a simple calculation done in our lab, the energy density of an 8 Ah polymer pouch cell is 25% greater than that of an 18650 equivalent. Thus, cells produced with higher capacities (up to 100 Ah) could be advantageous to the electric vehicle industry allowing for simpler manufacturing, reduced battery-management overhead, and increased driving ranges.

However, the desirable increase in size necessary to achieve high-capacity lithium ion cells contributes to the complexity of their inner-working and behavior. Large cells are typically composed of multiple thin layers of current collectors, separators, electrodes, and electrolyte materials. When particulate electrodes exhibit large volume expansions from lithiation, electrochemical shock and fracture can occur.[7] Distributed across large areas and multiple layers, this can cause erratic and unpredictable current pathways which lead to cell inhomogeneity. Inhomogeneity is undesirable because it can cause under-utilization of electrode materials and create local areas of overcharge and overdischarge. This in turn can ultimately reduce effective energy density and compromise cell safety and lifetime.

Past modeling efforts have predicted inhomogeneity in high capacity cells using multi-scale multi-dimensional modeling. [8] Additionally, numerous attempts have also been made to accurately model the phase transformation and voltage behavior for lithium iron phosphate batteries. [9-16] However, such modeling efforts are not sueful unless verified with experimental validation. Different attempts have been made to measure spatial variation and inhomogeneity in lithium ion batteries. Nanda *et al.* used Raman spectroscopy to map the state of charge of battery electrodes *ex situ*.[17] Liu *et al.* measured a large distribution of state of charge in a prismatic cell *ex situ* by synchrotron micro-diffraction.[18] Maire *et al.* provided state

of charge mapping using an in-situ colorimetry method.[19] Zhang *et al.* developed a cell with multiple electrode tabs in an attempt to track in-situ current distribution in a lithium ion cell. [20] Within the last year, X-ray absorption spectroscopy measurements carried out by Ouvrard *et al.* and Katayama *et al.* have shown inhomogeneous reaction distributions. [21,22] Their results point towards variance in conductive networks as the origin of inhomogeneity observed. However, the measurements are made in specially constructed experimental cells rather than manufactured product-type cells and they don't provide the resolution required for correlation to the voltage profile of the cell.

In this paper, we use a synchrotron white beam to conduct energy-dispersive x-ray diffraction (EDXRD) experiments in order to observe inhomogeneity in manufactured product-type high-capacity cells. EDXRD has proven to be a valuable tool for *in-situ* battery characterization.[23-25] Aided by ultrahigh photon energies, we are able to internally probe large lithium iron phosphate cells and collect diffraction spectra while discharging. By determining the relative amounts of non-lithiated and lithiated phases, we reveal the evolution of inhomogeneity with spatial and temporal resolution.

3.6 Experimental

3.6.1 Electrochemical cells

Two 8 Ah lithium iron phosphate polymer cells made on a manufacturing line were chosen for this study. The cells were constructed in a prismatic layout consisting of multiple repeating units of electrodes, current collectors, and separator materials. The positive electrodes were comprised of nano-sized lithium iron phosphate and were treated with a carbonaceous coating. The negative electrodes were composed of graphitic carbon. Both cells were cycled

approximately 1500 times with a 2C discharge rate and a 1C charge rate and were rested for two days before the experiment.

3.6.2 Energy-dispersive x-ray diffraction

The energy-dispersive X-ray diffraction experiments were carried out at the superconductiong wiggler beamline X17B1 of The National Synchrotron Light Source at Brookhaven National Laboratory in Upton, NY. The beamline provides a spectral flux with high brilliance across a range of energies up to 200 keV. The ultrahigh photon energies specifically allow for deep penetration in to the battery and minimal sample preparation; cells can be probed as-is. The cell was connected to a battery cycler (Arbin), and mounted to the sample stage. A germanium energy detector was fixed at 3° from the transmitted beam path. Bragg diffraction were measured in transmission (Laue) geometry, resulting in a fixed volume in space where diffraction occurs. A schematic is provided in Figure 3.1 Energy-dispersive synchrotron x-ray diffraction and the details of the beamline have been covered in this journal previously. [24]

The incident and detector collimating slits were arranged such to form a gauge volume with dimensions of approximately 3 mm x 3 mm x 40 µm. The height of the gauge volume is commensurate with that of the individual layers in the cell and allows for a proper resolution across the electrochemical interface.

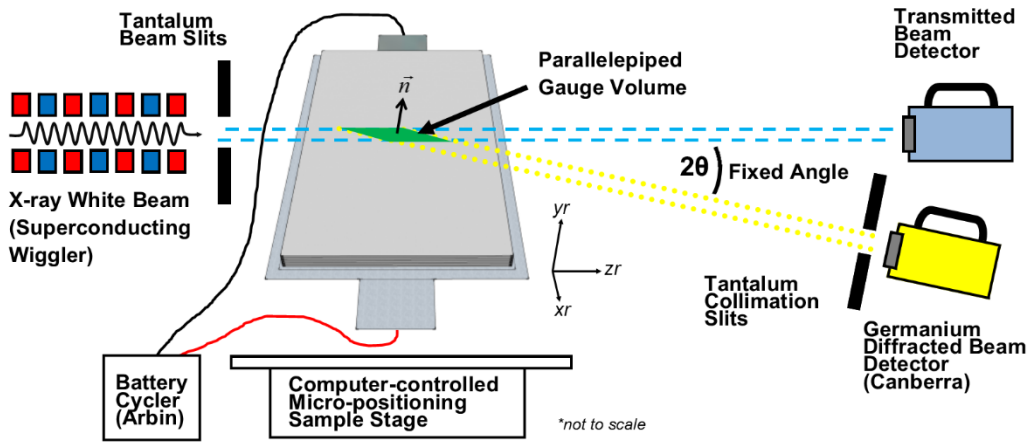

Figure 3.1 Energy-dispersive synchrotron x-ray diffraction

Schematic of the battery experiment at the X17B1 beamline at NSLS. Ultrahigh energy polychromatic x-rays are collimated through a series of slits and imposed on a battery which can move in all three dimensions. The transmission geometry gives way to a fixed volume in space where scattering is measured. The scattered x-rays are collected by a germanium energy detector after passing through collimating slits. The battery is connected to a cycler which is controlled by a computer.

3.6.3 Stoichiometric determination

In order to determine the relative amounts of $FePO_4$ and $LiFePO_4$ present in the gauge volume, a semi-quantitative peak-fitting routine was employed. The $FePO_4$ (020) and the $LiFePO_4$ (311) reflections were chosen for their high intensities and minimal overlap with other reflections. For each diffraction spectra, the aforementioned peaks, and surrounding peaks, were fit with a Gaussian function and their integrated intensity was determined. The formula used to estimate the weight fraction for each phase is given below:

$$\frac{W_\alpha}{W_\beta} = \frac{E_{\alpha,i}}{E_{\beta,j}} \frac{E^{rel}_{\beta,j}}{E^{rel}_{\alpha,i}} \frac{RIR_{\beta,c}}{RIR_{\alpha,c}}$$

where the W is the weight fraction, E is the measured intensity, E^{rel} is the relative intensity and RIR_c is reference intensity ratio to corundum. [26] For our analysis α is FePO4, β is LiFePO4, *i* is the 020 reflection and *j* is the 311 reflection. The reference intensity ratio (RIR_c and E^{rel}) values

were provided by Jade and calculated from FIZ#99861 (091109) for $FePO_4$ and calculated from FIZ#162282 (091109) for $LiFePO_4$. Because we knew that the sum of the weight fractions is unity, we then solved for the W_α. Lastly, by diving by their molecular weights, we solved the mole fraction of each phase. The mole fraction of the $FePO_4$ phase serves as a useful indicator for the local state of charge.

3.6.4 Measurement strategy

Entire mapping of a large cell would be time-prohibitive. So, in order to assess inhomogeneity, we devised two experimental conditions. First was to measure across the depth of an electrode interface located at the body-center of the cell. This was done in order to address variability in the yr-direction (See Figure 3.1 for coordinate system). A series of diffraction spectra were collected across a pair of positive and negative electrodes in a cyclic fashion as the cell was discharged at a constant current. The resulting *operando* data provide space and time mapping of the electrode during discharge.

In a complimentary fashion, to address variability in the yr-plane, nine points were chosen to compare across the battery. With the second cell initially at 60% state of charge, the nine locations were probed at the positive electrode in the center of the prismatic stack. The cell was then discharged for 1 hour at C4 rate and the nine locations were probed again. This process was repeated two more times with the last discharge time being 25 minutes when the cell reached 2.0 V. Overall, the nine locations were measured four times throughout the discharge process and the discharge process was paused while the measurements were taken. Special care was taken to make sure that the same electrode plane was probed each time. This was accomplished by calibration procedure that involves scanning in the yr-direction each time the area was measured.

3.7 Results and discussion

In order to properly track inhomogeneity, a basic understanding of the internal structure of the battery is required. Starting at the body-center of the cell, one unit of the repeating layer structure was analyzed by taking 10 measurements across with 40 micrometer resolution. Shown in Figure 3.2a, the data show both positive and negative electrode regions, divided by separators, with current collectors in the center of each electrode. The positive electrode is identified as lithium iron phosphate, the negative electrode as graphite, the positive collector foil as aluminum, and the negative foil as copper. A typical EDXRD spectra for the positive electrode is shown in Figure 3.2b.

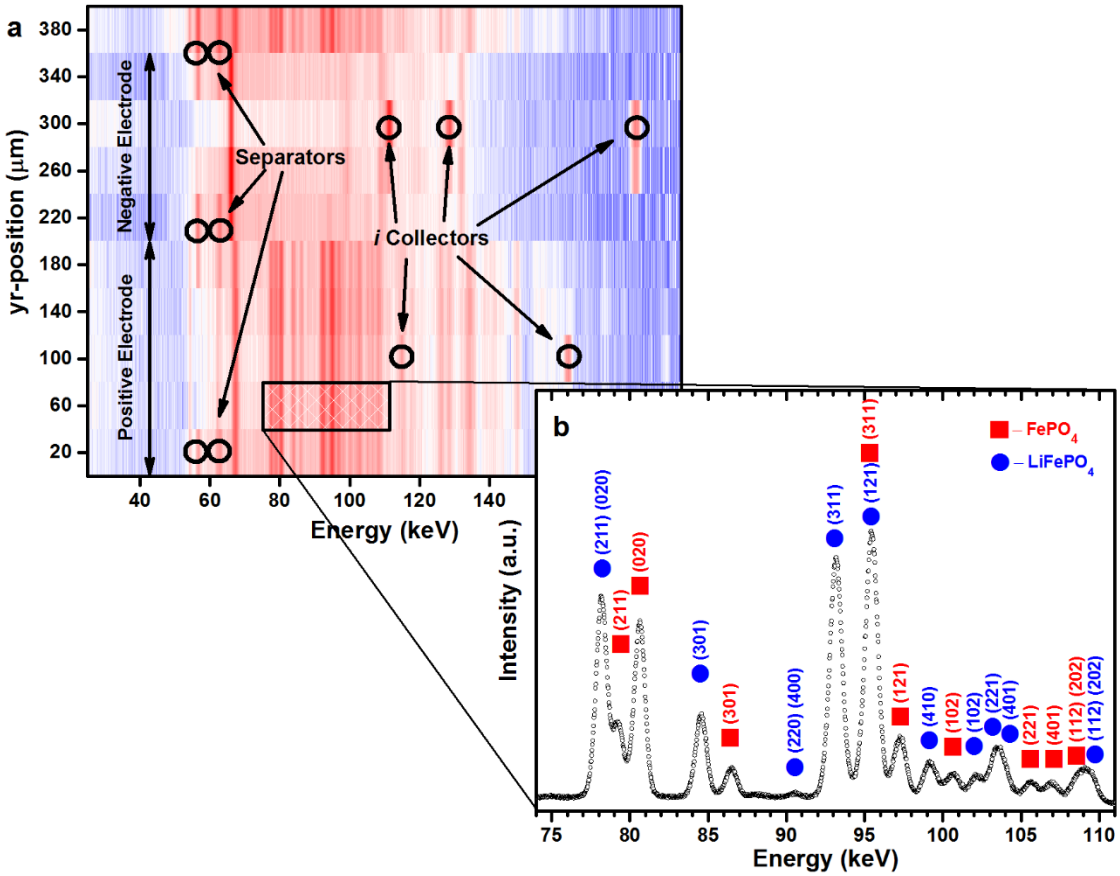

Figure 3.2 Internal phase mapping and structural information

a. Diffraction contour plot showing a one dimensional cross-section through an electrochemical cell. The region shown is one of approximately twenty repeating layers which comprise the cell. The contour plot is composed of ten diffraction spectra collected at 40 micrometer increments. Color represents the diffraction intensity with blue being the lowest and red being the highest. The current collectors are labeled and are coated on both sides with the respective electrode powders. **b.** Typical energy-dispersive diffraction spectrum of the lithium iron phosphate positive electrode. Upon lithiation, a new phase is created with a different crystal structure. This gives way to a juxtaposition of both diffraction patterns. The Bragg reflections of both phases are labeled by their *hkl* coordinates.

3.7.1 Depth profiling

Starting at approximately 75% of charge capacity, the cell was discharged at a C4 rate while scanning across the 400 micrometer section shown in Figure 3.2a. In total, 19 scans (where a scan is 10 spectra) were recorded operando as the cell was discharged. Focus was placed on the positive electrodes on either side of the current collector foil. Figure 3.3a shows the mole fraction for the $FePO_4$ phase as a function of position and location on the discharge curve which is shown in Figure 3.3b. The dashed lines represent the approximate locations of the negative electrodes and positive current collector. By tracking the local state of charge evolution on both sides of the current collector, Figure 3.3a clearly shows the behavior on one side of the collector that is different from the opposite side. It is important to note that we recorded three data points on one side of the collector and two points on the other. We believe that this doesn't mean the electrode thicknesses are different but that the gauge volume was slightly off center with respect to the current collector.

We also notice that at any given location in Figure 3.3a the response of the electrode is nonlinear. This is seen by the vertical spacing between each data point: as the cell is discharged, the spacing decreases, signifying that the local rate of reaction is slowing down. This asynchronous or delayed phenomenon has been observed before in numerous other $LiFePO_4$ studies. [27-30] One possible explanation for asynchronous behavior is a heterogeneous reaction and an x-ray probe volume which is not representative of the entire electrode. Our data supports this explanation showing that the asynchronous behavior is more pronounced on the side where the reaction range is more limited.

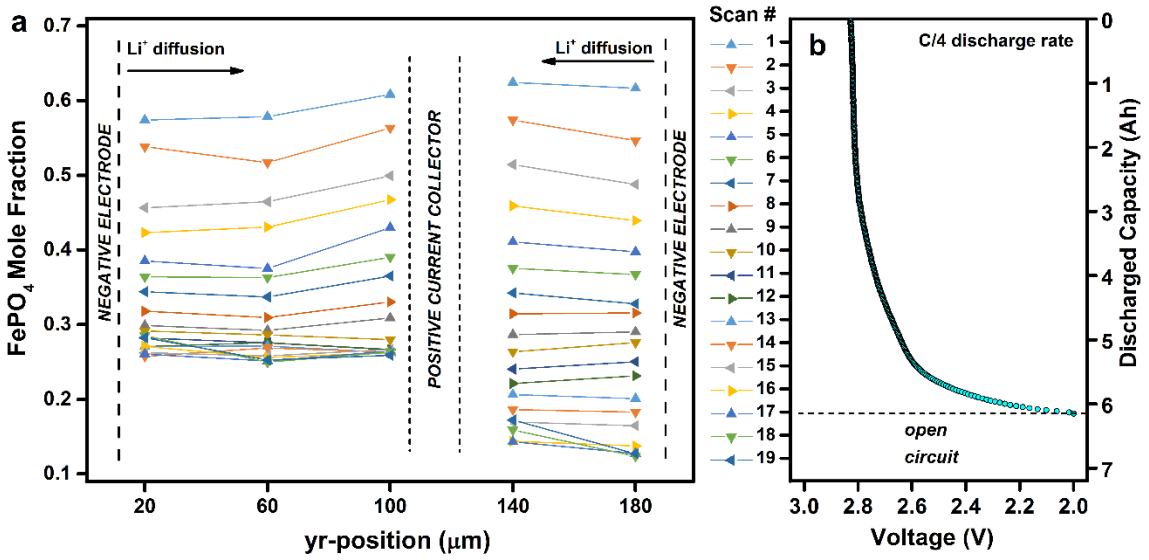

Figure 3.3 Operando electrode mapping

a. Time evolution of the iron phosphate mole fraction as a function of position (depth) in the electrode layer. As the cell is discharged, the iron phosphate phase is converted to lithium iron phosphate. The approximate locations for the positive current collector and negative electrodes are indicated. Lines are provided as a guide only. **b.** The cell potential as a function of capacity obtained while discharging the cell. The scan numbers on the left axis indicate the point at which each set of spectra were collected. Two scans were taken at open circuit after the discharge was halted.

The last two scans were taken after the cell finished discharging and was at open circuit voltage. It is important to point out that in Figure 3.3a at 20 µm and 140 µm, a phase relaxation is observed. That is that the local state of charge farthest from the current collector increases. This behavior has been observed before and suggests higher concentration of defects in those areas andor non-equilibrium conditions. [10,15,31]

Figure 3.3b shows a voltage plateau around 2.8 volts for the cell. We attribute the low voltage to a high internal resistance in the cell. Unfortunately, we did not collect voltage data after the discharge.

3.7.2 In-plane profiling

In order to characterize in-plane variability, nine points of interest were chosen and are shown in Figure 3.4a. Starting at about 60% of charge capacity, the nine points were tracked throughout the discharge process. The results, shown in Figure 3.4b, are very profound as the locally measured areas exhibit a high degree of inhomogeneity. Initially, all nine areas contain different local phase fractions. Once the discharge takes place, each location reacts at a different rate and the fastest are the locations (B, E, H) corresponding to the center of the cell, *e.g.* the space directly between the tabs.

Figure 3.4c shows the average of the ensemble measured at each discharge state. The behavior is strikingly linear. While a sample size of nine may not be statistically significant, it still reveals an important characteristic of the $LiFePO_4$ system: a linear behavior of the ensemble juxtaposed with an inhomogeneous behavior of local regions. In light of this, care should be taken when comparing macroscopic and microscopic measurements *e.g.* studies of cells probed *in situ* by x-ray techniques where chemical composition data are then compared to the electrical response of the cell. In these cases, the total volume of the material probed by x-rays is most

likely only a fraction of the volume of material contributing to the discharge curve. Therefore, extracting a $Li_{1-x}FePO_4$ line from the voltage curve and expecting a linear behavior in the chemical composition may result in asynchronous or delayed-discharge observation.

Most pronounced in the dataset is the delayed-discharge behavior of locations C and F. This behavior is characteristic lithium iron phosphate and is explained well by the resistive-reactant model originally proposed by Thomas-Alyea.[12] The model describes conductively coated LiFePO4 particles in terms of their inter- and intra-particle connectivity and proposes that they contribute in order of their conductivity. That is to say that the particles with the lowest electrical resistance react first and the ones with the highest resistance react last. Our observed behavior of locations C and F suggests that these areas have poorer electrical conductivity.

The standard deviation of the ensemble at different discharge states is shown in Figure 3.4d. The deviation increases as the cell is discharged but when completely discharged the deviation is at a minimum. The resistive-reactant model has been further investigated by Safari *et al*. through modeling experiments. [13] In their paper, they model four particle groups with varying amounts of conductivity and follow them independently during a discharge. In our data, Figure 3.4b and Figure 3.4d follow almost exactly the work of Safari *et al.* in Figure 11. They predict that the reaction networks formed through the heterogeneously connected particles is responsible for the path dependency of lithium iron phosphate batteries.

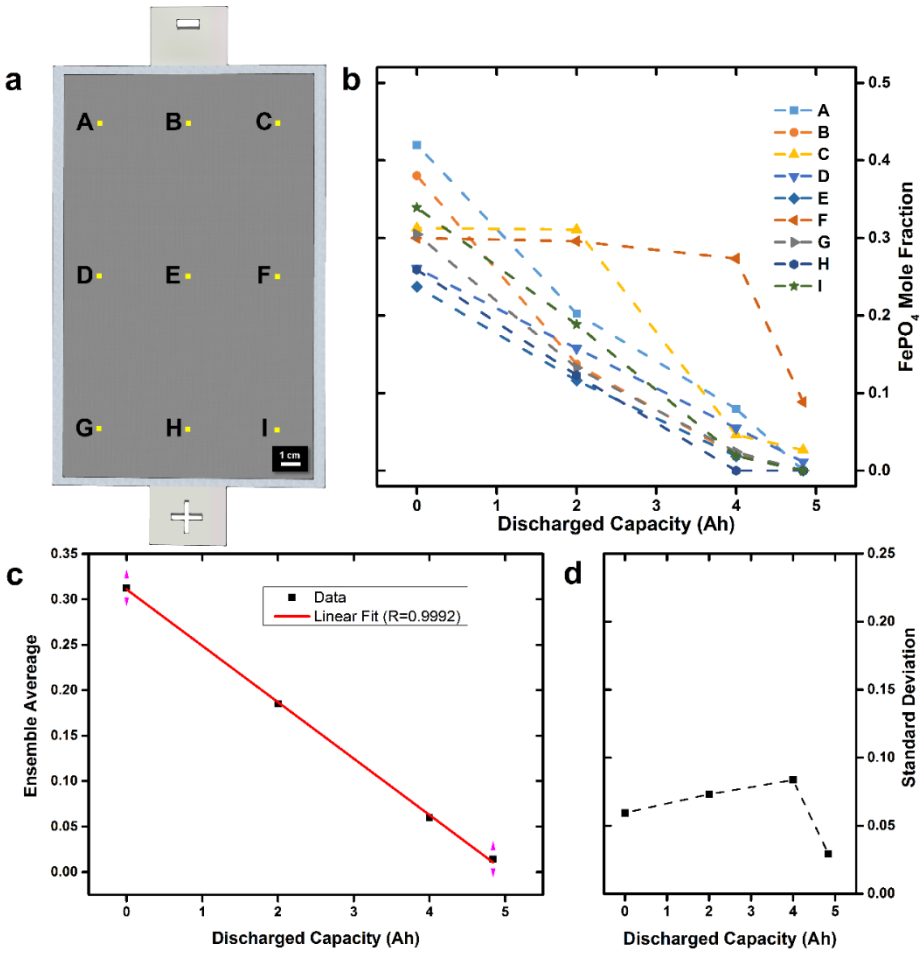

Figure 3.4 Spatial inhomogeneity while discharging

a. Schematic showing the locations of the battery that are probed. The yellow dots represent the area measured in the plane shown. **b.** Mole fraction of un-lithiated iron phosphate as a function of discharged capacity. As the cell is discharged the abundance of iron phosphate decreases. The mole fraction of iron phosphate can also be interpreted as the local state of charge in the cell. **c.** Evolution of the ensemble average as a function of discharged capacity. The data show extremely linear behavior with an R-value of 0.9992. **d.** Standard deviation of the ensemble versus discharged capacity

3.8 Conclusions

We have studied inhomogeneity in an 8 Ah high-capacity lithium iron phosphate cell using energy-dispersive x-ray diffraction with synchrotron radiation. Chemical composition was estimated through a reference intensity ratio method on the $LiFePO_4$ (311) and the $FePO_4$ (020) reflections. *Operando* electrode depth profiling was achieved during discharge conditions and revealed asynchronous discharge behavior and incomplete electrode utilization. Additionally, in-plane electrode measurements were made *in-situ* while the cell was discharged. Inhomogeneous behavior was observed across nine in-plane regions and a severely delayed discharge occurred at two of the regions. Ensemble behavior is linear suggesting the importance of micro- versus macro- observations. Overall, we attribute the inhomogeneous behavior to heterogeneous conductive coating on the particles as the data follows the resistive-reactant model closely.

3.9 Acknowledgements

The authors gratefully acknowledge Ankur Choksi, and Bart Visser for their support in the laboratory. The authors also acknowledge General Electric for the use of use of their battery cycler and their efforts in improving the beamline. Use of the National Synchrotron Light Source, Brookhaven National Laboratory, was supported by the U.S. Department of Energy, Office of Science, Office of Basic Energy Sciences, under Contract No. DE-AC02-98CH10886.

3.10 References

[1] B. Scrosati, J. Garche, Journal of Power Sources. 195 (2010) 2419-2430.

[2] Armand, Tarascon, Nature. 451 (2008) 652-657.

[3] W. Zhang, Journal of Power Sources. 196 (2011) 2962-2970.

[4] Padhi, Journal of The Electrochemical Society. 144 (1997) 1188.

[5] N. Ravet, Y. Chouinard, J.F. Magnan, S. Besner, M. Gauthier, M. Armand, Journal of Power Sources. 97–98 (2001) 503-507.

[6] Yamada, Chung, Hinokuma, Journal of The Electrochemical Society. 148 (2001) A224-A229.

[7] Ebner, Marone, Stampanoni, Wood, Science. 342 (2013) 716-720.

[8] Kim, Smith, Lee, Santhanagopalan, Pesaran, Journal of The Electrochemical Society. 158 (2011) A955-A969.

[9] Srinivasan, Newman, Journal of The Electrochemical Society. 151 (2004) A1517-A1529.

[10] Delmas, Maccario, Croguennec, Le Cras, Weill, Nature Materials. 7 (2008) 665-671.

[11] G.K. Singh, G. Ceder, M.Z. Bazant, Electrochimica Acta. 53 (2008) 7599-7613.

[12] K.E. Thomas-Alyea, ECS Transactions. 16 (2008) 155-165.

[13] Safari, Delacourt, Journal of The Electrochemical Society. 158 (2011) A63-A73.

[14] Safari, Delacourt, Journal of The Electrochemical Society. 158 (2011) A562-A571.

[15] Malik, Zhou, Ceder, Nature Materials. 10 (2011) 587-590.

[16] Farkhondeh, Safari, Pritzker, Fowler, Han, Wang, Delacourt, Journal of the Electrochemical Society. 161 (2013) A201-A212.

[17] J. Nanda, J. Remillard, A. O'Neill, D. Bernardi, T. Ro, K.E. Nietering, J. Go, T.J. Miller, Advanced Functional Materials. 21 (2011) 3282–3290.

[18] Liu, Kunz, Chen, Tamura, Richardson, The Journal of Physical Chemistry Letters. 1 (2010) 2120-2123.

[19] Maire, Evans, Kaiser, Scheifele, Novák, Journal of The Electrochemical Society. 155 (2008) A862.

[20] Zhang, Shaffer, Wang, Rahn, Journal of the Electrochemical Society. 160 (2013) A610-A615.

[21] G. Ouvrard, M. Zerrouki, P. Soudan, B. Lestriez, C. Masquelier, M. Morcrette, S. Hamelet, S. Belin, A.M. Flank, F. Baudelet, Journal of Power Sources. 229 (2013) 21.

[22] M. Katayama, K. Sumiwaka, R. Miyahara, H. Yamashige, H. Arai, Y. Uchimoto, T. Ohta, Y. Inada, Z. Ogumi, Journal of Power Sources. 269 (2014) 999.

[23] Scarlett, Madsen, Evans, Coelho, McGregor, Rowles, Lanyon, Urban, Journal of Applied Crystallography. 42 (2009) 502-512.

[24] J. Rijssenbeek, Y. Gao, Z. Zhong, M. Croft, N. Jisrawi, A. Ignatov, T. Tsakalakos, Journal of Power Sources. 196 (2011) 2332-2339.

[25] Takeuchi, Marschilok, Takeuchi, Ignatov, Zhong, Croft, Energy & Environmental Science. 6 (2013) 1465.

[26] R.L. Snyder, Powder Diffraction. 7 (1992) 186-193.

[27] H. Chang, C. Chang, H. Wu, M. Yang, H. Sheu, N. Wu, Electrochemistry Communications. 10 (2008) 335-339.

[28] Leriche, Hamelet, Shu, Morcrette, Masquelier, Ouvrard, Zerrouki, Soudan, Belin, Elkaïm, Baudelet, Journal of The Electrochemical Society. 157 (2010) A606-A610.

[29] Wang, Jaye, Nam, Zhang, Chen, Bai, Li, Huang, Fischer, Yang, Journal of Materials Chemistry. 21 (2011) 11406.

[30] H.C. Shin, K.W. Nam, W.Y. Chang, B.W. Cho, W. Yoon, X. Yang, K.Y. Chung, Electrochimica Acta. 56 (2011) 1182-1189.

[31] Park, Kameyama, Yao, Electrochemical and Solid-State Letters. 15 (2012) A49-A52.

4. Asynchronous stoichiometric response in lithium iron phosphate batteries

4.1 Preface

This chapter is based on a paper published in the Journal of Materials Research. (*J. Mater. Res.*, (2015)). The full list of authors includes William A. Paxton, Enver Koray Akdoğan, Ilyas Şavkliyildiz, Ankur U. Choksi, Scott X. Silver, Zhong Zhong, and Thomas Tsakalakos. The role of William A. Paxton was to design and perform all experiments, process and analyze all data, and prepare the manuscript for submission.

4.2 Abstract

Operando energy-dispersive x-ray diffraction (EDXRD) was carried out on a newly-formed 8 Ah lithium iron phosphate ($LiFePO_4$) battery with the goal of elucidating the origin of asynchronous phase transformation commonly seen with *in-situ* x-ray diffraction studies. The high-energy photons at the NSLS X17B1 beamline allow for penetration in to a fully-assembled battery and therefore negate any need for a specially-designed *in-situ* cell which often uses modified current collectors to minimize x-ray attenuation. Spatially-and-temporally resolved phase-mapping was conducted with a semi-quantitative reference intensity ratio (RIR) analysis to estimate the relative abundance of the de-lithiated phase. The data show an asynchronous response in the stoichiometry versus the electrochemical profile and suggest limited diffusion in the electrode towards the end of discharge. Our results confirm that the asynchronous electrode response is not just limited to specially-designed cells and occurs in fully-assembled production line cells alike. We attribute this behavior to be a consequence of performing a local measurement over a wide-area heterogeneous reaction.

4.3 Introduction

The use of lithium-ion batteries in portable electronics has enabled a proliferation of devices in recent years. Still, the large scale present-and-future requirements of energy storage for transportation and grid applications are not yet met by available technologies. Specifically, energy density, power capability, cycle life, calendar life, and safety all need improvement. Low-cost manufacturing will also be required for lithium-ion batteries to compete with existing power infrastructure. [1-3]

One of the main hindrances in the progress of battery research is that the constituent electrode materials are inaccessible once an electrochemical cell is constructed. This leaves the researcher with a limited number of available feedback mechanisms to assess the cell's performance, e.g., current, voltage, and impedance. Indeed, there is a whole scientific community dedicated to the study and modeling of such electrochemical data. [4] However, these data are limited in their ability to reveal the more-localized smaller-scale structural mechanisms on which the batteries' performance is so dependent. [5]

In the last 20 years great advancement has been made in the area of *in-situ* characterization using x-rays, enabling researchers to study battery materials without removing them from a cell. Aside from improvements in probe brightness and detector efficiency, these advancements can largely be credited to the construction of new cell designs utilizing low-absorption encapsulation and current-collector materials, thus allowing for greater penetration of x-rays. Such work has enabled discovery of hidden phases and the screening of potential future electrode materials. [6-9]

Of those materials, olivine structured lithium iron phosphate, $LiFePO_4$, shows great promise as an electrode, due to its superior thermal stability, relatively-low cost, and high capacity

retention during cycling. [10-13] Despite intrinsically low electronic and ionic conductivity, its use in commercial batteries has become a reality through the engineering of particle morphology and composition. [10-13] Still, the exact nature of the phase transformation during lithiation is elusive, despite many theoretical and in-situ studies. [14]

It is understood that the phase transformation upon lithiation of $FePO_4$ is first-order which gives way to a characteristic flat voltage response and biphasic composition with very limited solid solution regions at the end-member phases. [10-14] This has been confirmed by a multitude of in-situ studies of the lithiation and de-lithiation processes in which researchers have compared structural measurements to the electrochemical response. [15-17] Disregarding the limited solid-solution ranges, one can consider the equation $\mathrm{FePO_4 + Li^+ + e^- \rightleftarrows LiFePO_4}$. This shows that for each lithium ion that intercalates, an electron is generated and the lithiated phase is created. However, in some cases anomalous behavior has been observed; that is to say that after extracting X% of the electrons from the system, the phase fraction observed deviates far from X%. [18-23] There are quite a few explanations of this so-called asynchronous phase transition behavior, ranging from effects of polaron formation in the lattice [14] to the existence of a non-representative x-ray volume measured in a heterogeneous electrode. [23-24] While both are possible, the most recent modeling efforts [25] and the work of others [16], suggest that heterogeneous microstructure and electrical conductivity of the electrode plays a large role in the phase transformation behavior.

Energy-dispersive x-ray diffraction (EDXRD) is well-established as a viable tool for in-situ battery characterization. [26-30] Additionally, recent studies utilizing synchrotron radiation have shown very powerful spatial-and-temporal mapping capabilities. [28-30] The ultrahigh energy x-rays available (up to 200 kev) from the X17 super-conducting-wiggler beamport at the National Synchrotron Light Source give way to low absorption losses and enable *operando*

measurements. [28-30] Here, we use the term *operando* to differentiate the ability of EDXRD to take measurements in fully-assembled cells without special sample preparation. In this paper we use the unique *operando* spatial and temporal mapping capabilities of EDXRD to study the response of a lithium iron phosphate electrode in an actual production battery. We intend to elucidate any spatial effects which may contribute to the asynchronous phase transition behavior.

4.4 Experimental

The lithium-ion battery that was chosen for this *operando* study was a fully-assembled 10 Ah lithium iron phosphate polymer cell. In order to achieve a capacity of 10 Ah, the internal structure of the cell consisted of multiple repeating units of electrodes, current collectors, and separator materials in a prismatic layout. The positive electrodes were comprised of nano-sized lithium iron phosphate which were coated in carbon for increased electrical conductivity. The negative electrode consisted of graphitic carbon. The cell was recently assembled with no prior history, besides formation cycles, and was therefore considered new.

X-ray diffraction measurements were conducted at the superconductiong wiggler beamline X17B1 of The National Synchrotron Light Source at Brookhaven National Laboratory. The superconducting wiggler provides a spectral flux with high brilliance across a wide range of energies up to 200 keV. [31] In an energy-dispersive x-ray diffraction measurement the Bragg condition for diffraction is satisfied by the use of polychromatic radiation, therefore allowing measurements at a fixed angle. Experiments were carried out in Laue geometry which results in a fixed diffraction volume in space, commonly referred to as the gauge volume (GV), with a parallel-piped geometry. Figure 4.1 gives a schematic of the configuration.

The governing equation for EDXRD is given by

$$E_{hkl} = \frac{6.199}{\sin\theta \, d_{hkl}}$$

where *E* is energy in keV and d_{hkl} is the interatomic spacing associated with the plane *hkl* measured in Angstroms. The photons are collected and their energy is measured using a germanium detector. The photon counts are then binned in to 8192 channels using a multi-channel analyzer. The energy calibration is done later by the use of LaB_6 and CeO_2 standards.

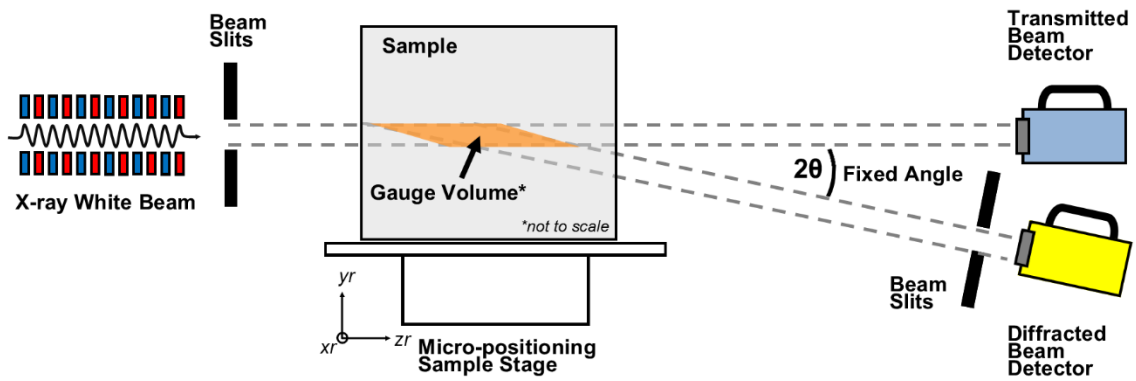

Figure 4.1 Experimental configuration of the X17B1 beamline at NSLS.

The high energy polychromatic x-rays are collimated through a series of slits and imposed on a sample which can move in all three dimensions. Within the gauge volume, the material scatters the x-rays where they are collected by an energy detector at a fixed angle.

A Bragg angle of 2θ = 3° was used and the slits were arranged such that a gauge volume with dimensions of approximately 3 mm x 3 mm x 30 µm is formed. The 30 µm height of the gauge volume gives rise to a thickness that is commensurate with that of the individual electrode layer in the cell. This is important for phase-mapping ability because one is able to obtain a distinct signal from one electrode layer rather than multiple layers. The battery was carefully placed and leveled on a sample holder that can move in x, y, and z directions with

accuracy of 0.1 µm. The orientation of the cell placement with respect to the beam is shown in Figure 4.2a. A very accurate tomographic profile of the cell was obtained and served as a map of the internal structure of the cell. This is achieved by scanning the gauge volume through the entire thickness of the cell and then plotting the total scattered intensity as a function of position. Such a plot was used to calibrate the experiment and locate an area of interest. The tomographic profile is shown, along with the area of interest, in Figure 4.2b. With the cell fully charged, a sequence of 15 diffraction spectra were collected as a function of depth in the yr-direction. The area of study was in the body-center of the cell and the collection time for each spectrum was 45 seconds. Using a battery cycler (Arbin BT2000), the cell was then discharged at a constant current of 2 amperes which corresponds to a C-rate of C5. Every 45 minutes, the discharge procedure was halted and, after a relaxation time of 5 minutes, depth profiles were taken. This procedure was repeated throughout the discharge cycle for a total collection of nine depth profiles.

The relative amounts of $FePO_4$ and $LiFePO_4$ phases were determined semi-quantitatively using a Gaussian peak-fitting routine found in the software, fityk. [32] The $FePO_4$ (020) and the $LiFePO_4$ (311) reflections were chosen because they had the best combination of intensity and isolation from any other reflection. However, surrounding reflections were also fit in order to isolate their contributions. Additionally, since the gauge volume is much larger than the crystallites measured, we assume there to be no texture related effects and a single reflection to be a good representation of the phase as a whole. The integrated intensities (area under the curve) of each peak were used to compute the weight fractions of each phase using the reference intensity ratio (RIR) method. [33] In this analysis, the ratio of the intensities are weighted using their reference values (I_{rel}) and their ratio to a known standard of corundum (RIR_c) shown in the following equation. The I_{rel} and RIR_c values used for the analysis were 62.72

and 1.49 for $FePO_4$ [34], and 92.75 and 1.32 for $LiFePO_4$ [35] respectively. The mole fraction can then be calculated by dividing the weight fraction by the molar mass. Furthermore, showing the mole fraction of the $FePO_4$ phase can be a convenient indicator of the remaining capacity in the volume measured, thereby leading to a spatially-resolved phase mapping. [24] It is also important to note, since the analysis compares two phases within each spectrum, it negates any need to consider current-decay effects from the synchrotron ring when comparing different locations and time-points as long as the signal strength is sufficiently above the experimental noise as it was throughout the experiments.

After the synchrotron experiment, the fully-discharged cell was disassembled in an argon-filled glove box. The approximate area of interest was cut away and mounted to a sample-stud using carbon tape. Images were taken for analysis using a field-emission scanning electron microscope (Zeiss).

4.5 Results and Discussion

A summary of the measurements collected from the battery is shown in Figure 4.2. As previously mentioned, Figure 4.2a shows the orientation of the cell with the beam, and 2b shows the tomographic profile of internal layered structure. Figure 4.2c shows a diffraction contour plot with energy on the x-axis and position on the y-axis. In this plot, the cathode and anode regions of the cell are indicated as are the characteristic Bragg lines of the current collectors. The cathode region is identified as a two-phase mixture of $FePO_4$ and $LiFePO_4$. Also in the cathode region is an aluminum current collector. The anode region can be seen with much fewer lines; identified as lithiated graphite and a copper current collector. We assume there to be some curvature of the electrode layers which would explain the small juxtaposition of the

current collector and electrode phases. Figure 4.2d shows selected diffraction spectra from the contour map with the Bragg peaks of both lithiated and non-lithiated phases identified.

The cell potential curve during discharge is shown in Figure 4.3. The numbers indicate the points at which the discharge was halted and diffraction spectra were collected. The cell provided a flat voltage profile which is indicative of the first-order phase transformation. Small drops in the voltage can be seen when the discharge starts after each scan which is caused by the internal resistance of the cell. The overall capacity of the cell is what we expected.

A more detailed phase mapping of the positive electrode is shown in Figure 4.4. Here we show the space-time evolution of the electrode with the $FePO_4$ mole fraction as a function of depth in the electrode. As the cell is discharged, the iron phosphate phase is converted to lithium iron phosphate by the diffusion of lithium ions in to the cathode from the electrolyte, with an accommodating change of valence state of the Fe in the lattice. The variation of composition as a function of depth appears to be relatively linear in most scans. The only pronounced area where it is not is in scan number 8 where the edge closest to the separator and anode (lithium source) is fully lithiated. This shows evidence of lower diffusion mobility towards the later part of the discharge. Based on these data, it is not possible to say what exactly is limiting diffusion, but the fact that the diffusion mobility is only observed towards the end of the battery's discharge cycle, coinciding with where there is a larger deviation from equilibrium voltage, suggests that the two may be correlated. This is consistent with the model used by *Farkhondeh et al.* for bulk behavior dominated by heterogeneous conductive coatings on a poor electronic conductor. [25]

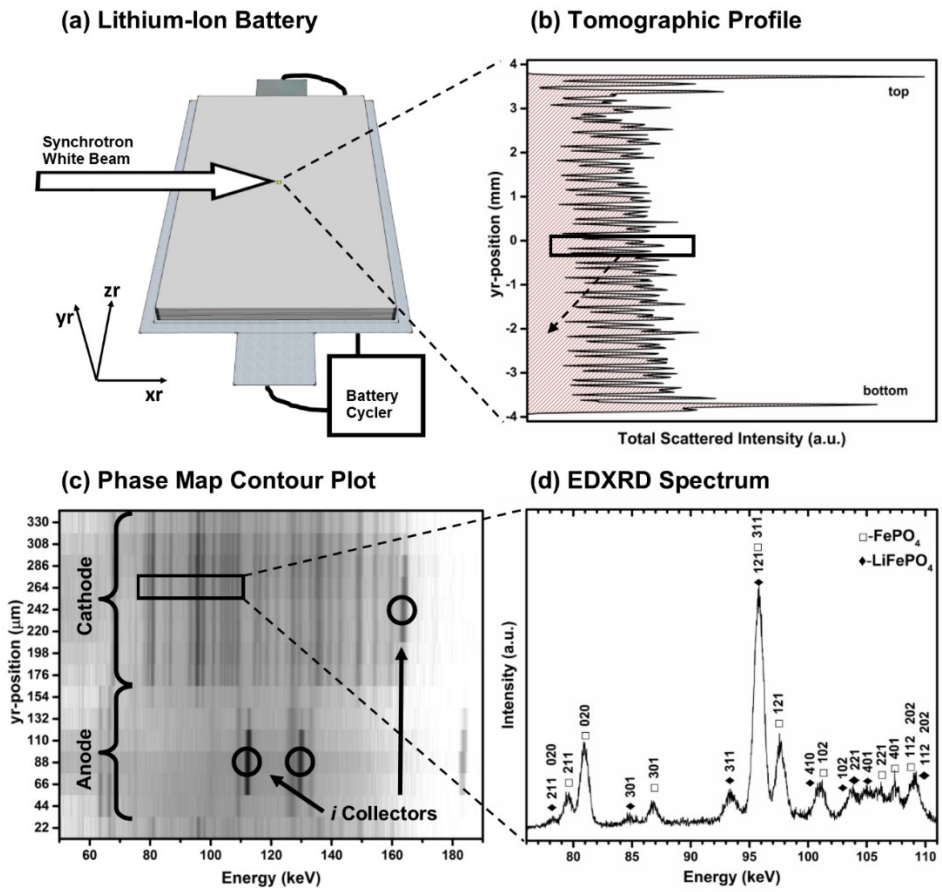

Figure 4.2 Summary of the characterization capabilities of energy-dispersive x-ray diffraction as they relate to lithium-ion batteries.

a. Depiction of the lithium-ion battery in relation to the synchrotron beam along with the experimental coordinates. The cell is also connected to a battery cycler. **b.** A tomographic profile of the internal structure of the cell is shown by plotting the total scattered intensity as a function of position. The plot is rotated to remain consistent with the experimental coordinates. **c.** A contour plot of the scans across a selected region inside the cell is given for the purpose of phase mapping. The electrodes of the cell are identified as well as the current collectors. **d.** A single energy-dispersive x-ray diffraction spectrum of an area within the cathode region. The Bragg reflections of two phases are labeled.

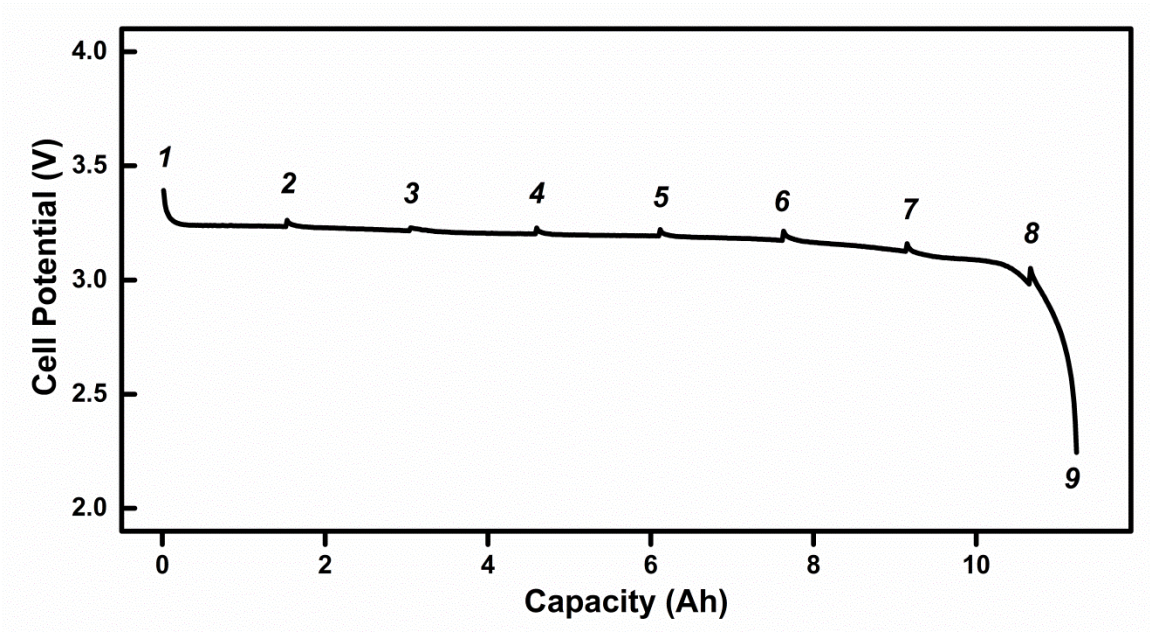

Figure 4.3 The cell potential as a function of capacity obtained when discharging the cell.

The times at which the discharge was stopped and diffraction spectra collected are indicated by the numbers above the curve.

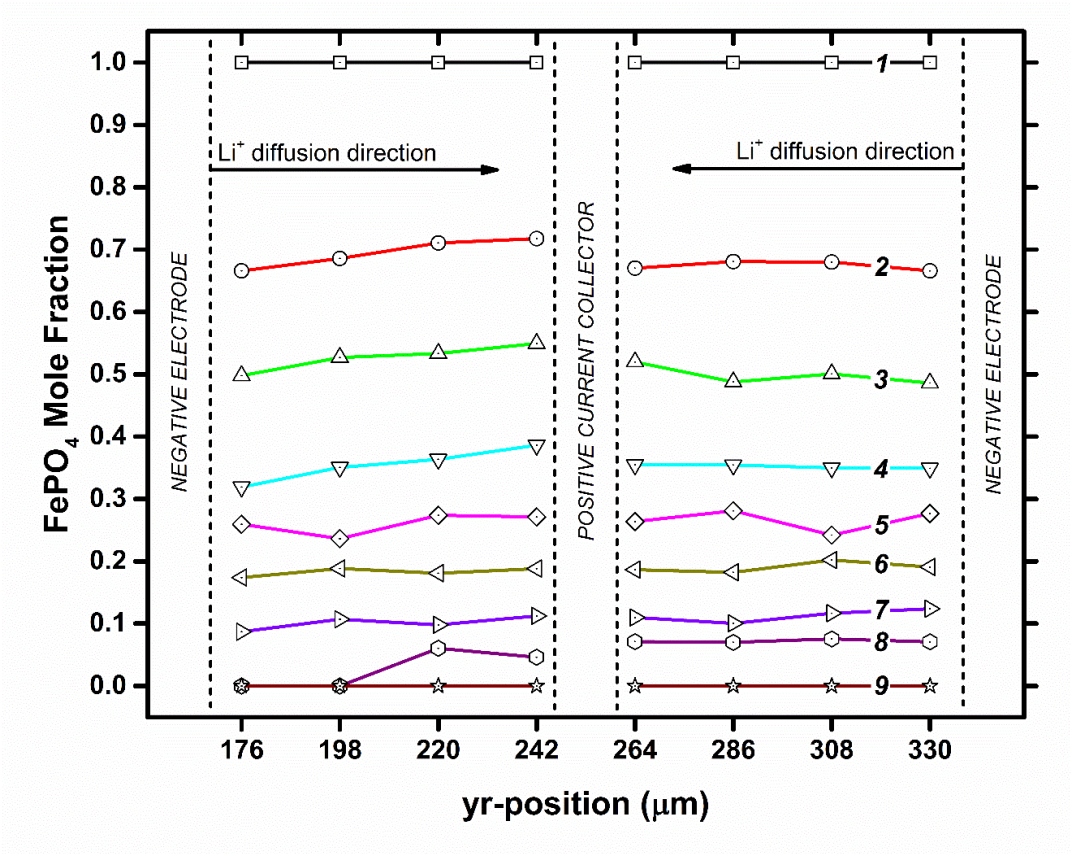

Figure 4.4 Time evolution of the iron phosphate mole fraction as a function of position (depth) in the electrode layer.

As the cell is discharged, the iron phosphate phase is converted to lithium iron phosphate by the diffusion of lithium ions in to the positive electrode from the negative electrode. The numbers of the lines indicate the time depicted in

The data in Figure 4.4 also show a deviation from ideal-stoichiometric behavior in the electrode, similar to that of the previously-hypothesized asynchronous phase transformation. Since the cell was discharged at a constant current and the diffraction spectra were taken at equal intervals, we expected to see a linear response in the transformation of $FePO_4$ to $LiFePO_4$; a 1:1 relationship of Li^+ to e^-. However, after the first discharge interval, the amount of $FePO_4$ converted to $LiFePO_4$ was approximately 30%. This number appears to decrease as the battery is discharged further. Additionally, the time and space mapping shows that the observed asynchronous electrode utilization phenomenon appears consistent throughout the depth of the electrode. Since the effect is consistent throughout the electrode, we decided to plot just the evolution of both phases in the region in electrodes center. This is shown in Figure 4.5 where the asynchronous response can be seen more clearly. A waterfall plot of the nine diffraction spectra used for the RIR analysis is shown in Figure 4.6. The peaks used for analysis, $FePO_4$ 020 at ~81 keV and $LiFePO_4$ 311 at ~93 keV, are labeled and show suitable intensity for the analysis.

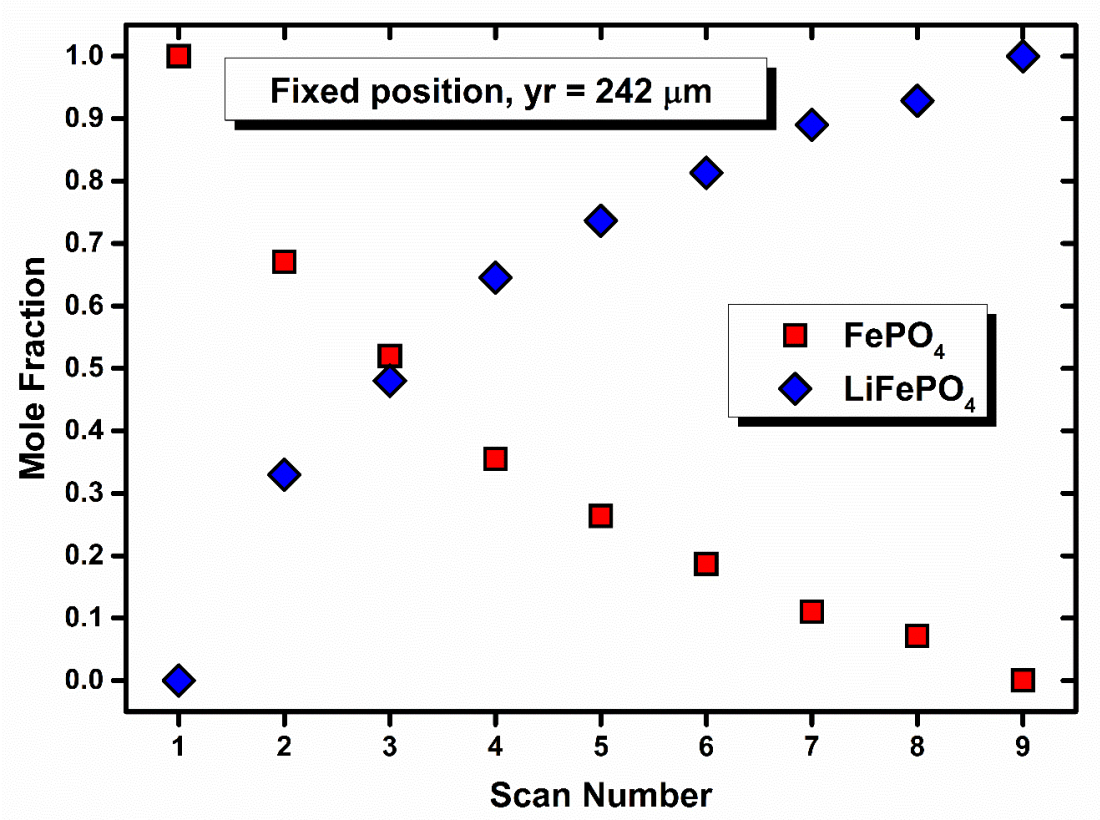

Figure 4.5 Mole fraction of $FePO_4$ and LiFePO4 phases at the position which is centrally located in the electrode.

The measured fractions of each phase show the asynchronous electrode utilization behavior.

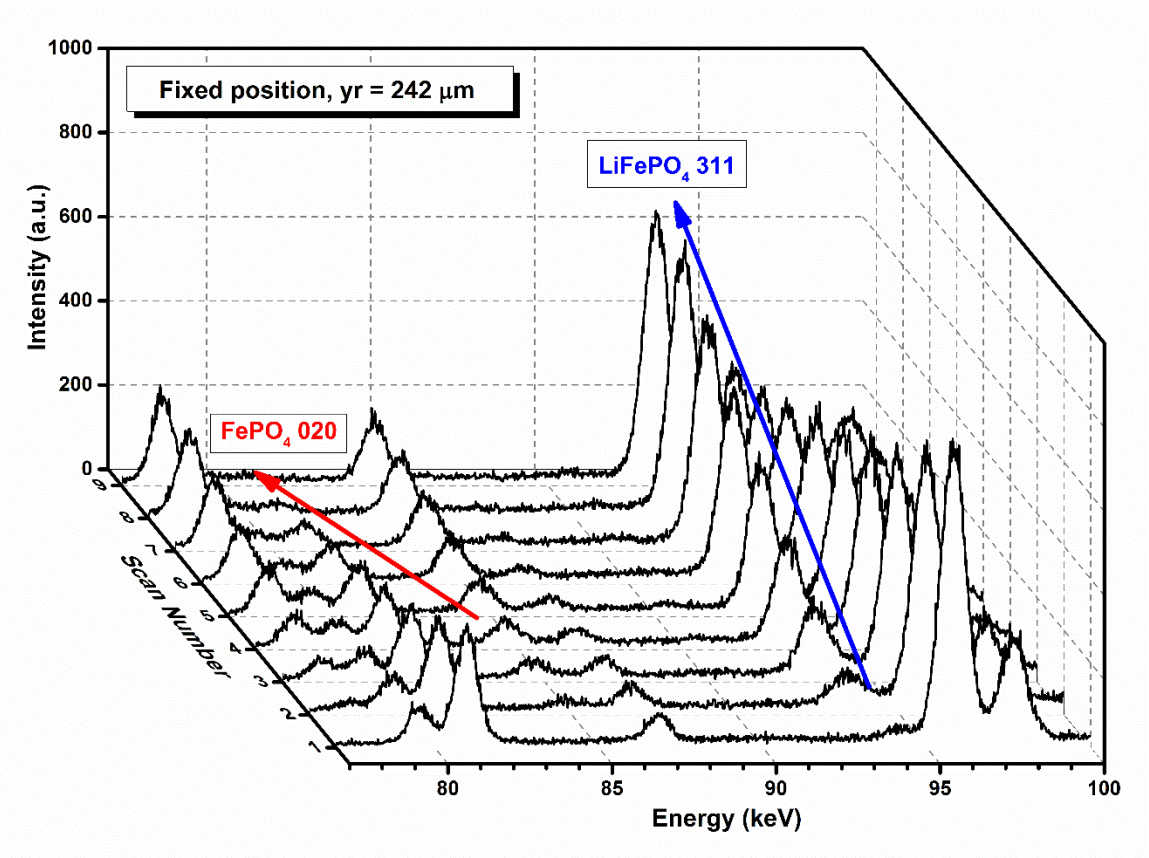

Figure 4.6 Waterfall plot of the 9 spectra collected in a fixed position at 242 µm, which is approximately the center of the electrode depth.

The FePO4 (020) and LiFePO4 (311) peaks are labeled, indicating the reflections used for the mole fraction analysis.

Figure 4.7 shows a field-emission scanning electron micrograph of the positive electrode from the disassembled sample. The iron phosphate cathode powder appears to have nano-sized grains but also larger grains and agglomerations. Additionally, the particles appear to be quite heterogeneous with a fairly broad size distribution and varying morphologies. Evidence of fracturing also suggests the presence of electrochemical-induced strains which can occur from the volume changes associated with lithium intercalation. We postulate that the material heterogeneity contributes to a spatially-heterogeneous reaction-front within the electrode, thus influencing a localized asynchronous response.

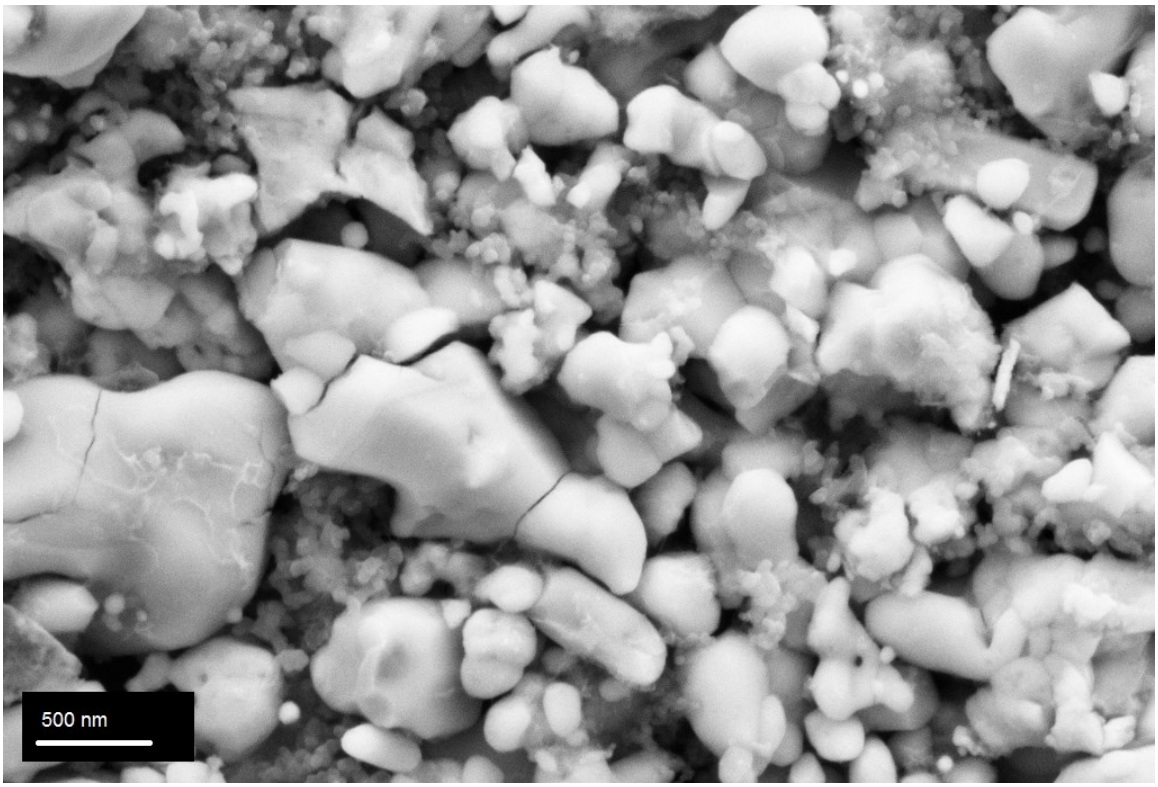

Figure 4.7 Scanning electron micrograph of the positive electrode.

The sample was obtained by disassembling the fully-discharged cell under a glove box and cutting away the area of the cell that was measured. The image shows a heterogeneous powder with fractured grains and a broad size distribution.

While we observe the asynchronous electrode response, the origins of which still remain elusive. We postulate that the asynchronous response is a localization phenomenon, the result of variances in the electrode/electrolyte/current-collector interfaces and/or the surface treatments of the particles. This is certainly possible considering the measurements presented in this study represent less than 1% of the total contributing electrode. Powder heterogeneity observed by electron microscopy further corroborates a localization phenomenon. However, additional experiments are required to fully determine the origin of asynchronous behavior. Further experiments where we investigate different areas of the cell are under way. If we observe the asynchronous response in one area and a complimentary behavior in another, we may be able to confirm that it is a localization phenomenon caused by heterogeneous microstructure and conductive contact, provided that the areas average out to a more linear electrode response.

4.6 Concluding Remarks

We have conducted *operando* energy-dispersive x-ray diffraction measurements on a full-sized lithium iron phosphate battery and a succinct overview of the measurement capabilities is given. Spatially and temporally resolved phase mapping was achieved at nine different time points while discharging the battery. A mole fraction phase analysis using the reference intensity ratio method was completed for the positive electrode. The results show limited diffusion towards the end of the discharge cycle as well as an asynchronous electrode utilization response. The results confirm that the asynchronous behavior is not just an artifact of in-situ cell designs and occurs in fully-assembled batteries as well. We attribute this behavior to be a consequence of performing a local measurement over a wide-area heterogeneous reaction.

4.7 Acknowledgements

Use of the National Synchrotron Light Source, Brookhaven National Laboratory, was supported by the U.S. Department of Energy, Office of Science, Office of Basic Energy Sciences, under Contract No. DE-AC02-98CH10886.

4.8 References

[1] M. Armand and J. M. Tarascon, Nature. 451 (2008) 652-657.

[2] B. Scrosati and J. Garche, J. Power Sources. 195 (2009) 2419-2430.

[3] J. R. Croy, A. Abouimrane, and Z. Zhang: MRS Bull. 39 (2014) 407.

[4] T. B. Reddy, Linden's Handbook of Batteries, Fourth Edition. McGraw-Hill, New York, NY (2011).

[5] M. Ebner, F. Marone, M. Stampanoni and V. Wood, Science 342 (2013) 716-720.

[6] J. N. Reimers and J. R. Dahn, J. Electrochem. Soc. 139(8), 2091-2097, (1992).

[7] G. G. Amatucci, J. M. Tarascon and L. C. Klein, J. Electrochem. Soc. 143 (1996) 1114-1123.

[8] M. Morcrette, Y. Chabre, G. Vaughan, G. Amatucci, J.-B. Leriche, S. Patoux, C. Masquelier, and J.-M. Tarascon, Electrochim. Acta 47 (2002) 3137-3149.

[9] M. A. Rodriguez, D. Ingersolla, S. C. Vogel and D. J. Williams, Electrochem. Solid-State Lett. 7 (2004) A8-A10.

[10] A. K. Padhi, K. S. Nanjundaswamy, and J. B. D. Goodenough, J. Electrochem. Soc,. 144 (1997) 1188-1194.

[11] A. Yamada, S. C. Chung and K. Hinokuma, J. Electrochem. Soc. 148 (2001) A224.

[12] S-Y Chung, J. T. Bloking, and Y-M Chiang: Electronically conductive phospho-olivines as lithium storage electrodes. Nature Mater. 1(2), 123-128, (2002).

[13] W-J. Zhang: Structure and performance of LiFePO4 cathode materials: A review. J. Power Sources 196(6), 2962-2970, (2011).

[14] Corey T. Love, Anna Korovina, Christopher J. Patridge, Karen E. Swider-Lyons, Mark E. Twigg and David E. Ramaker. J. Electrochem. Soc. 160 (2013) A3153-A3161.

[15] A. S. Andersson, B. Kalska, L. Haggstrom and J. O. Thomas, Solid State Ionics 130 (2000) 41-52.

[16] C. Delmas, M. Maccario, L. Croguennec, F. Le Cras and F. Weill, Nature Mater. 7 (2008) 665-671.

[17] N. Meethong, Y.-H. Kao, M. Tang, H.-Y. Huang, W. C. Carter and Y.-M. Chiang,Chem. Mater. 20 (2008) 6189-6198.

[18] H-H. Chang, C-C. Chang, H-C. Wu, M-H. Yang, H-S Sheu and N-L Wu, Electrochem. Commun. 10 (2008) 335-339.

[19] H. C. Shin, K. Y. Chung, W. S. Min, D. J. Byun, H. Jang and B. W. Cho, Electrochem. Commun. 10 (2008) 536-540.

[20] K. Inoue, S. Fujieda, K. Shinoda, S. Suzuki and Y. Waseda, Mater. Trans. 51 (2010) 2220-2224.

[21] J. B. Leriche, S. Hamelet, J. Shu, M. Morcrette, C. Masquelier, G. Ouvrard, M. Zerrouki, P. Soudan, S. Belic, E. Elkaïm and F. Baudelet, J. Electrochem. Soc., 157 (2010) A606-A610.

[22] H. C. Shin, K. W. Nam, Y. W. Chang, B. W. Cho, W-S. Yoon, X-Q. Yang and K. Y. Chung, Electrochim. Acta, 56 (2011) 1182–1189.

[23] X-J. Wang, C. Jaye, K-W. Nam, B. Zhang, H-Y. Chen, J. Bai, H. Li, X. Huang, D. A. Fischer and X-Q. Yang, J. Mater. Chem., 21 (2011) 11406-11411.

[24] J. Liu, M. Kunz, K. Chen, N. Tamura and T. J. Richardson, J. Phys. Chem. Lett. 1 (2010) 2120-2123.

[25] M. Farkhondeh, M. Safari, M. Pritzker, M. Fowler, Taeyoung Han, Jasmine Wang and C. Delacourt, J. Electrochem. Soc., 161 (2014) A201-A212.

[26] F. Ronci, B. Scrosati, V. Rossi Albertini and P. Perfetti, Electrochem. Solid-State Lett., 3 (2000) 174-177.

[27] S. Panero, P. Reale, F. Ronci, B. Scrosati, P. Perfetti and V. Rossi Albertini, Phys. Chem. Chem. Phys. 3 (2001) 845-847.

[28] J. Rijssenbeek, Y. Gao, Z. Zhong, M. Croft, N. Jisrawi, A. Ignatov, and T. Tsakalakos, J. Power Sources, 196 (2011) 2332-2339.

[29] E. Takeuchi, A. Marschilok, K.Takeuchi, A. Ignatov, Z. Zhong, and M. Croft, Energy Environ. Sci., 6 (2013) 1465-1470.

[30] J. W. Gallaway, C. K. Erdonmez, Z. Zhong, M. Croft, L. A. Sviridov, T. Z. Sholklapper, D. E. Turney, S. Banerjee and D. A. Steingart, J. Mater. Chem. A, 2 (2014) 2757-2764.

[31] W. Thomlinson, D. Chapman, N. Gmür, N. Lazarz, Nucl. Instrum. Meth. A, 266(1988) 226-233.

[32] M. Wojdyr, J. Appl. Cryst., 43 (2010) 1126-1128.

[33] F. H. Chung, J. Appl. Cryst., 8 (1975) 17.

[34] Calculated from FIZ#99861 (091109) by Jade for $FePO_4$

[35] Calculated from FIZ#162282 (091109) by Jade for $LiFePO_4$

4.9 Supplemental Figures

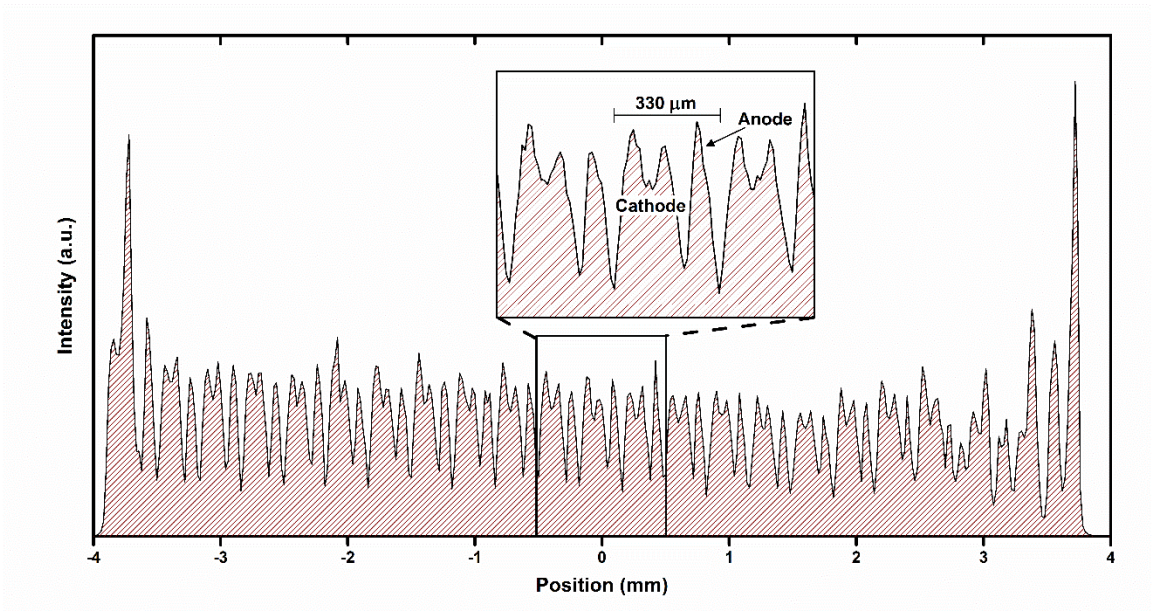

Figure 4.8 A tomographic profile of the battery is produced by plotting the total scattered intensity as a function of position.

Here the gauge volume was moved through the center of the battery. The multi-layer construction of the cell becomes apparent and the relative dimensions are easily measured.

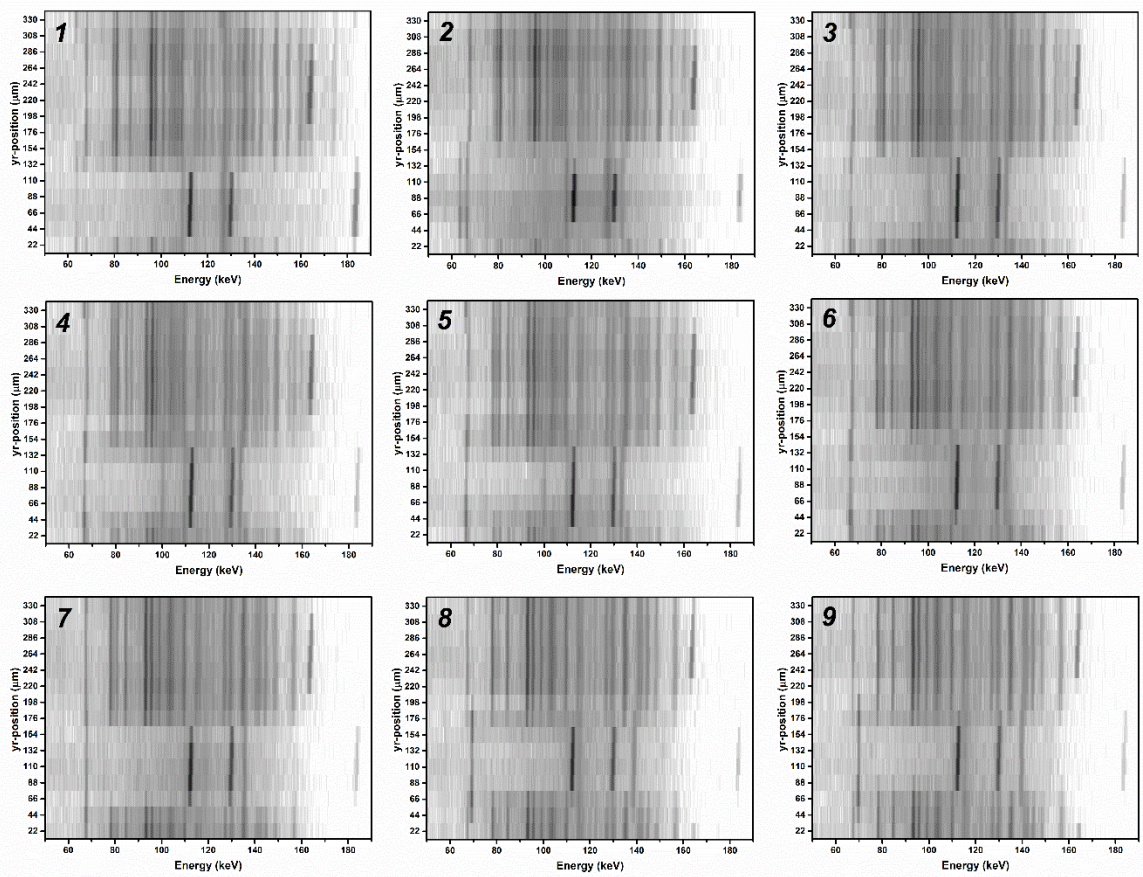

Figure 4.9 Phase map contour plots for each time point.

5. Additional Data

5.1 Preliminary evidence for inhomogeneity

The experimental objective was to measure the topological variation in state of charge. Two commercial 8 Ah lithium iron phosphate cells were chosen for the study. Sample 1 was a virgin cell and sample 2 had been cycled 1045 times at a rate of C2 charge and C2 discharge. The cells were then measured in 9 different locations as shown in Figure 5.1. The dimensions of each location were roughly 3mm × 5mm × 40µm and located in the center of the electrode stack. For each area a diffraction pattern was collected for 60 seconds.

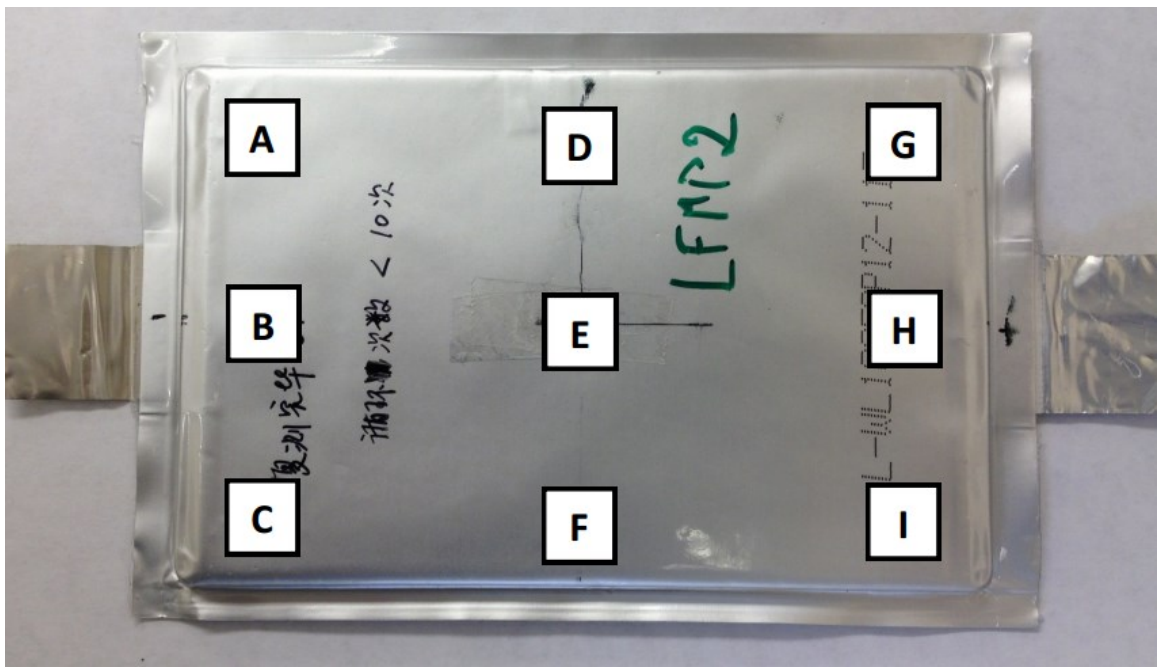

Figure 5.1 Locations measured in topological study

For analysis the 301 peaks of both FP and LFP phases were identified and fit to a Gaussian profile shape function. The intensity ratios between FP and LFP were calculated along with the error and are presented in Figure 5.1. Unfortunately, when measuring sample 2, there was a technical error that prevented data collection on the last point, location I.

The data show that there is a large degree of variability of SOC over different positions of the cell. There is no recognizable pattern in the variability however. The mean and standard deviation are presented in Table 5.1 and for sample 2 there was a larger degree of variation. The increased variation could be attributed to the increased number of cycles on the sample 2, however further studies would be needed to determine.

Table 5.1 State of charge measurements

Sample	History	Mean (std. dev.)	Max.	Min.
1	New, after formation	18% (9.038)	31.1%	3.8%
2	1045 cycles	37.1% (9.778)	55.7%	22.7%

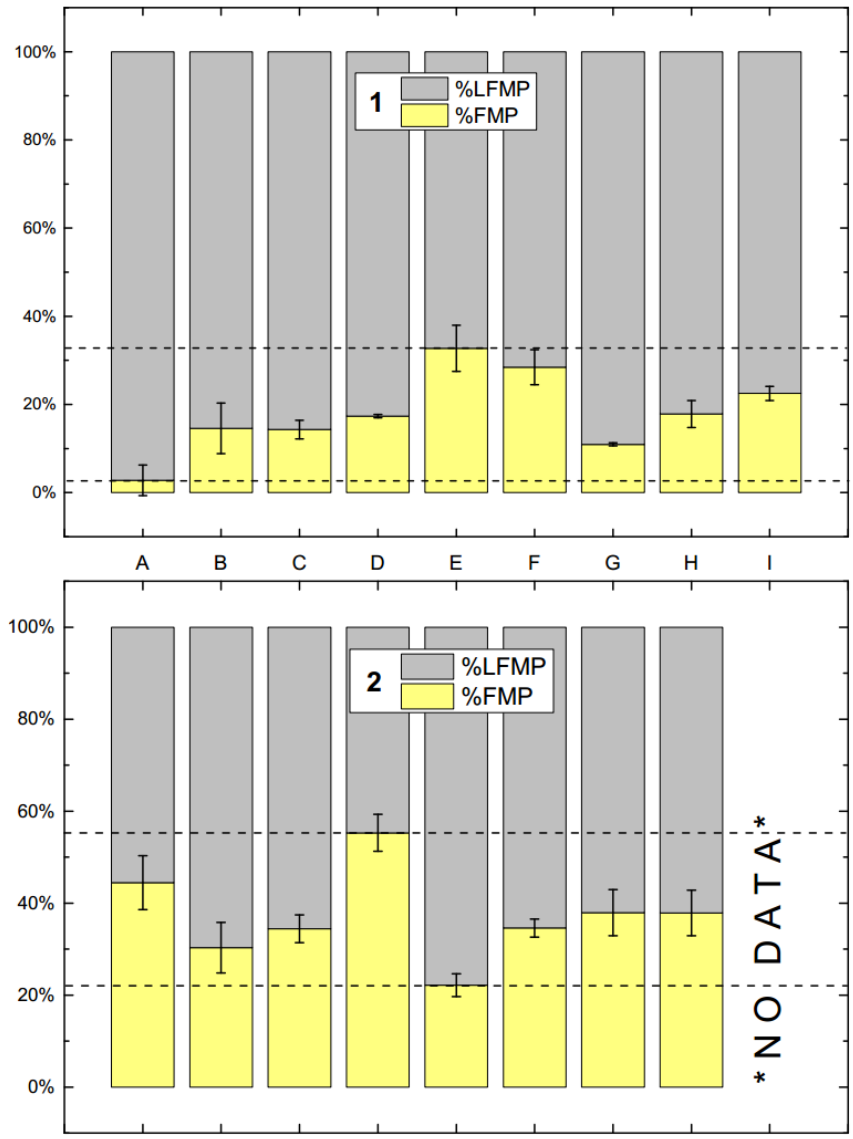

Figure 5.2 Topological variation of state of charge for two batteries

5.2 CR2032 and BR2032 Coin Cells

5.2.1 Preface

CR2032 and BR2032 coin cells were studied using energy dispersive x-ray diffraction at the NSLS X17-B1 beamline. The cells were discharged by 20% and 40% (depth of discharge) at both fast and slow rates. Cells were then mapped in the yr-direction (thickness) with 50 micrometer resolution. A semi-quantitative peak fitting routine was employed to determine relative amount of lithiated and non-lithiated phases present. Concentration profiles of the phases were then determined as a function of depth in the electrode, rate, and depth of discharge.

5.2.2 Electrochemical Cells

The batteries chosen for the study were CR2032 and BR2032 primary lithium cells manufactured by Panasonic Corporation. The CR cells are composed of MnO_2 cathode and the BR cells are composed of the CF_x cathode. For each battery type, five cells were prepared. A cell was measured as-is, both fast and slow discharges to 20% and 40% depths respectively. Table 5.2 gives a full depiction of how the cells were prepared.

Table 5.2 List of samples used for the study

Cell ID	Cathode type	Discharge current	Discharge depth
CR-AS-IS	MnO_2	0	0
CR-F5	MnO_2	5 mA	20%
CR-S5	MnO_2	0.5 mA	20%
CR-F8	MnO_2	5 mA	40%
CR-S7	MnO_2	0.5 mA	40%
BR-AS-IS	CF_x	0	0
BR-F1	CF_x	2.5 mA	20%
BR-S3	CF_x	0.25 mA	20%
BR-F1	CF_x	2.5 mA	40%
BR-S3	CF_x	0.25 mA	40%

5.2.3 Slit settings

The incident and detector collimating slits were arranged such to form a gauge volume with dimensions of approximately 3 mm x 3 mm x 50 µm.

5.2.4 Data analysis

The EDXRD data was analyzed using a graphical peak-fitting software. The MnO2 and LiMnO2 peaks were fit using a Gaussian peak shape and the CFx peaks were fit using a Lorentzian peak shape.

5.2.5 Results and Discussion

5.2.5.1 Lithium Manganese Dioxide

Figure 5.3 shows the EDXRD spectra for both the lithiated and non-lithiated phases of MnO_2. In red, the non-lithiated phase is determined to be the gamma phase of MnO_2. This phase exhibits broad peak widths, indicative of a fine nanometer-scale particle size. When comparing to the lithiated phase, the spectra shown in blue has some sharper peaks in the lower energies but similar peak widths in the higher energies. The peaks are labeled to the best of knowledge and those used for analysis are indicated with stars.

The concentration was estimated by comparing the integral peak width of the lithiated phase to the sum of integral peak widths of the lithiated and non-lithiated phases. The concentration depth profiles are shown in Figure 5.4. The data shows a well-defined reaction front that propagates through the depth of the electrode. At 0% depth of discharge (DoD), there is already a reaction front at the edge of the electrode. This is expected as the manufacturer most likely “primes” the cells before they ship them out. At 20% DoD, the front has moved deeper in to the electrode and at 40% DoD deeper still. A kinetic effect is observed when comparing the two discharge rates. The faster discharge kinetics leaves a more sharply defined

reaction front. The slower discharge allows for deeper penetration in to the depth of the electrode.

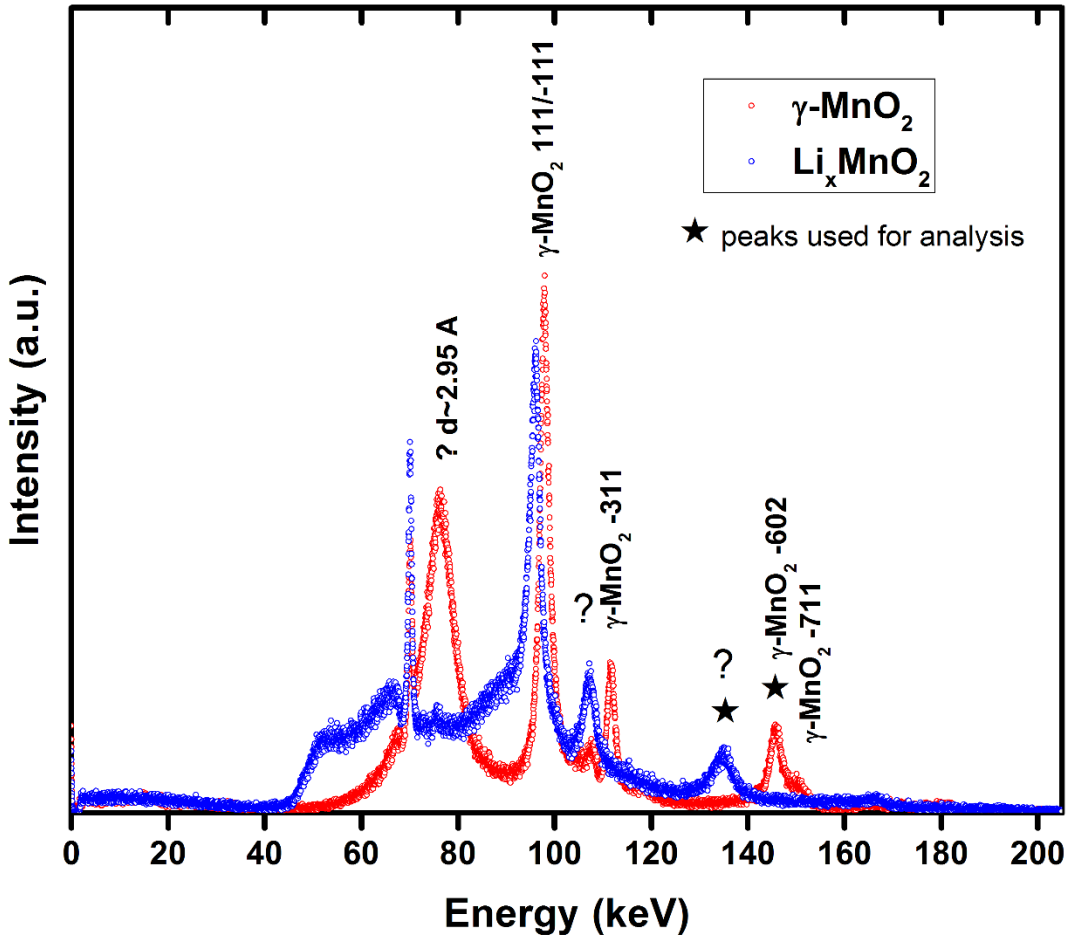

Figure 5.3 EDXRD spectra of both lithiated and non-lithiated MnO_2

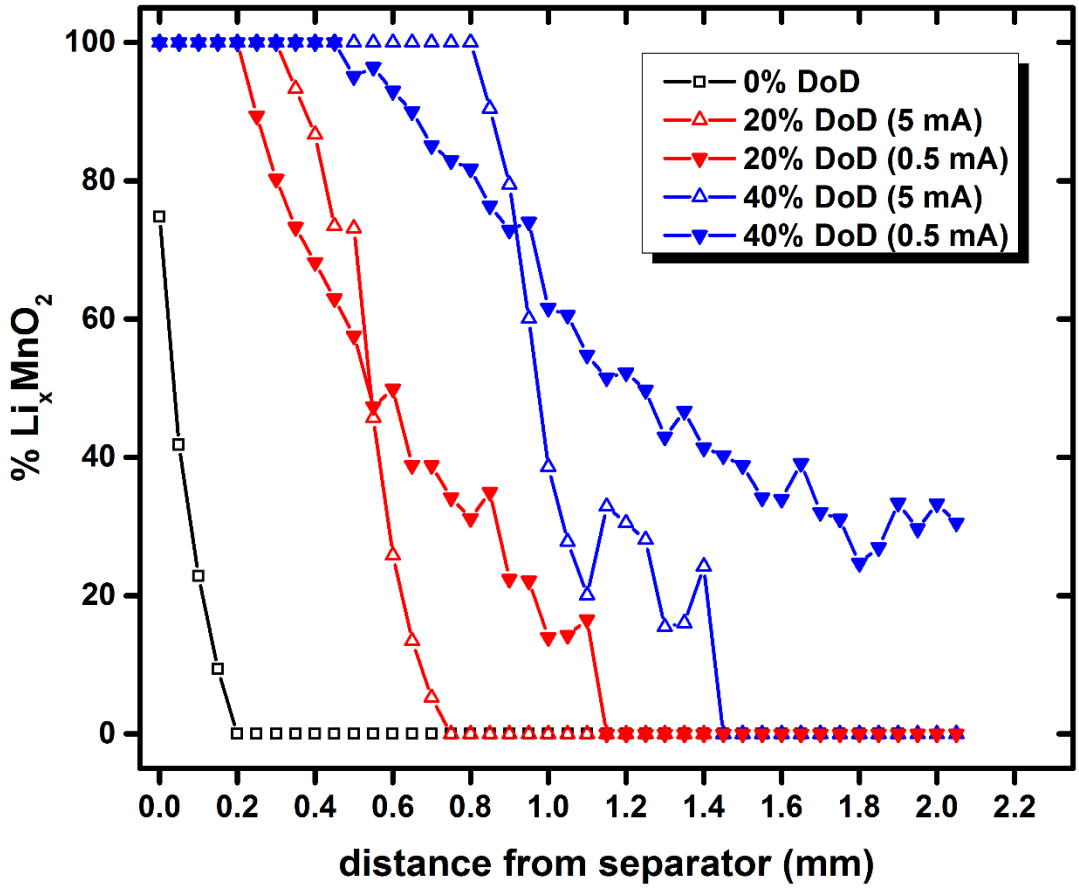

Figure 5.4 Li_xMnO_2 depth profiles

5.2.5.2 Lithium Carbon Monoflouride

Figure 5.5 shows the EDXRD spectra for the CFx and LiF+C phases. Both phases exhibit large broad peaks in the lower energy regions. The CFx phase has a broad peak around 110 keV in contrast to the sharply defined LiF 111 and 200 peaks around 100 keV and 118 keV respectively. Specific reflections were identified and labeled for the LiC and C phases, however CFx reflections were not easily labeled to their hkl planes. The two peaks chosen for analysis are indicated in the spectra with stars.

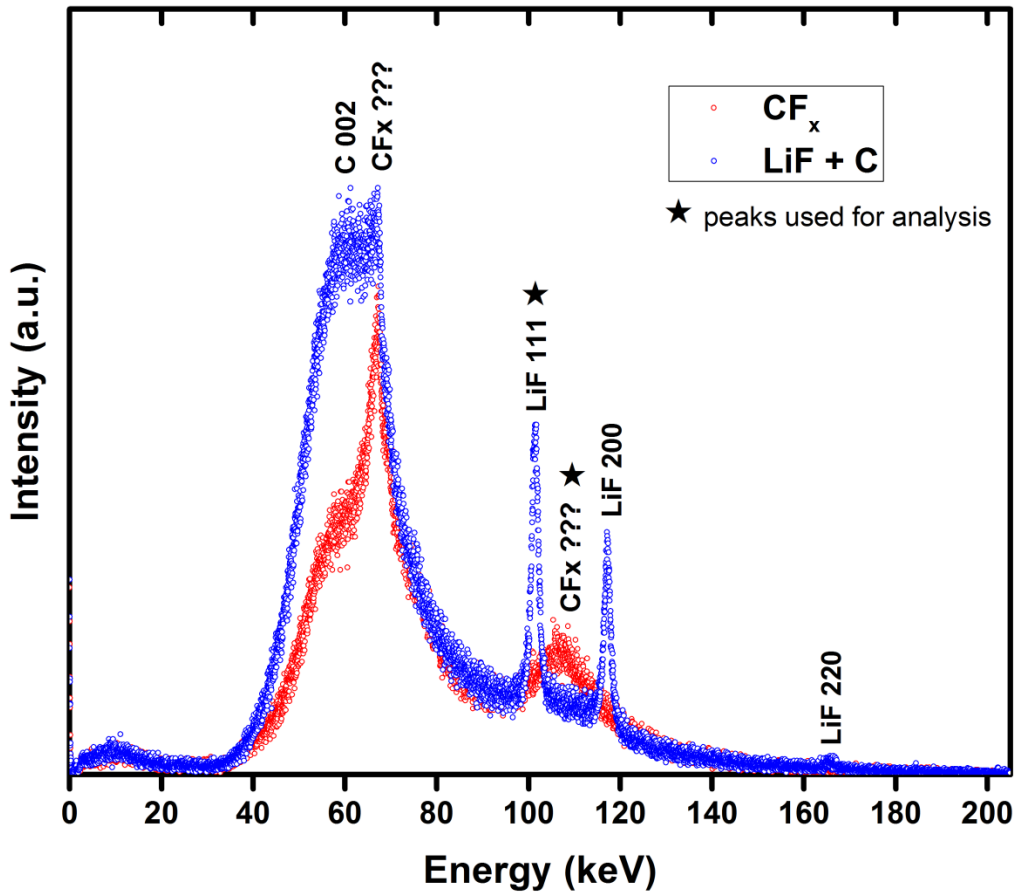

Figure 5.5 EDXRD spectra of both CF_x and LiF+C phases

The concentration of LiF was estimated in the same manner described in section 5.2.5.1. The concentration depth profiles are shown in Figure 5.6. The figure shows a reaction front that remains close to the edge of the electrode but with utilization of the entire electrode exhibited as an exponential decay towards the far edge. At the far edge of the electrode, the concentration of LiF is an approximate indicator of the depth of discharge. Comparing the rate effects, at faster rates the slope of the concentration curve is steeper than the slower rates.

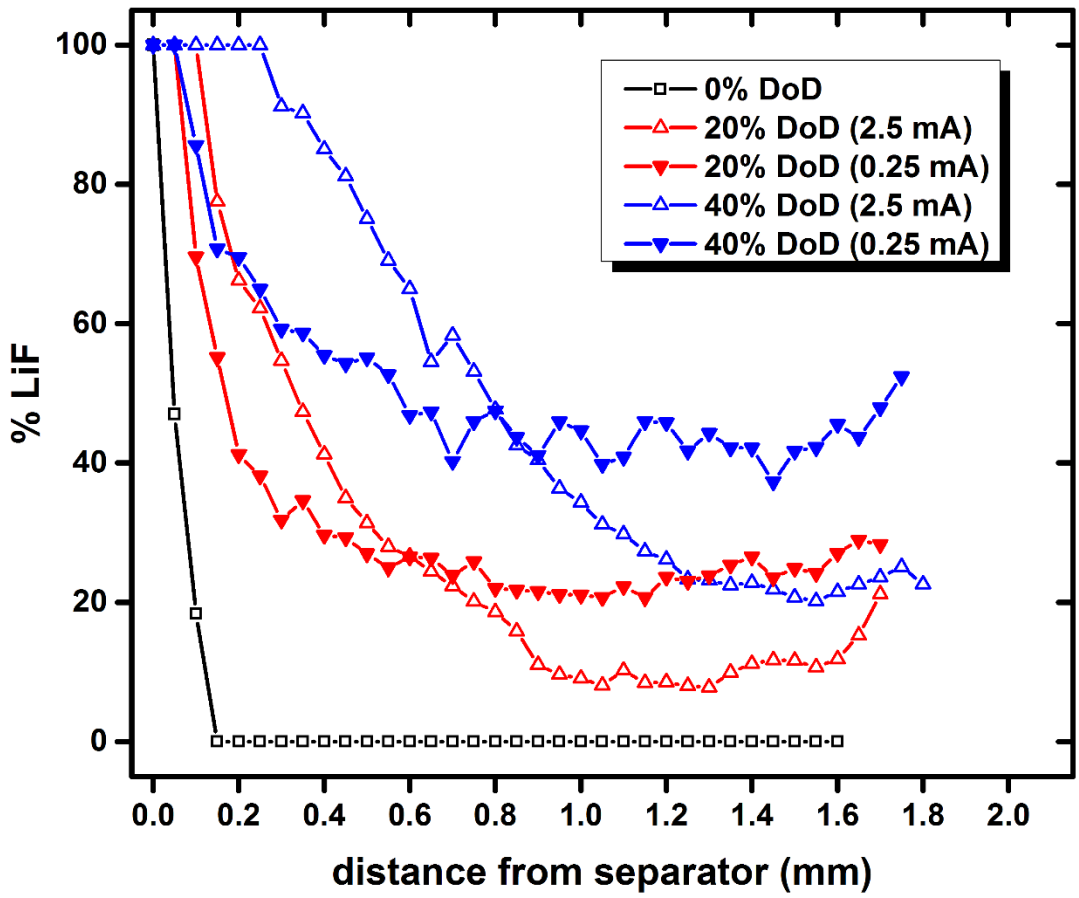

Figure 5.6 Depth profiles of LiF phase

5.2.5.3 Phase Maps

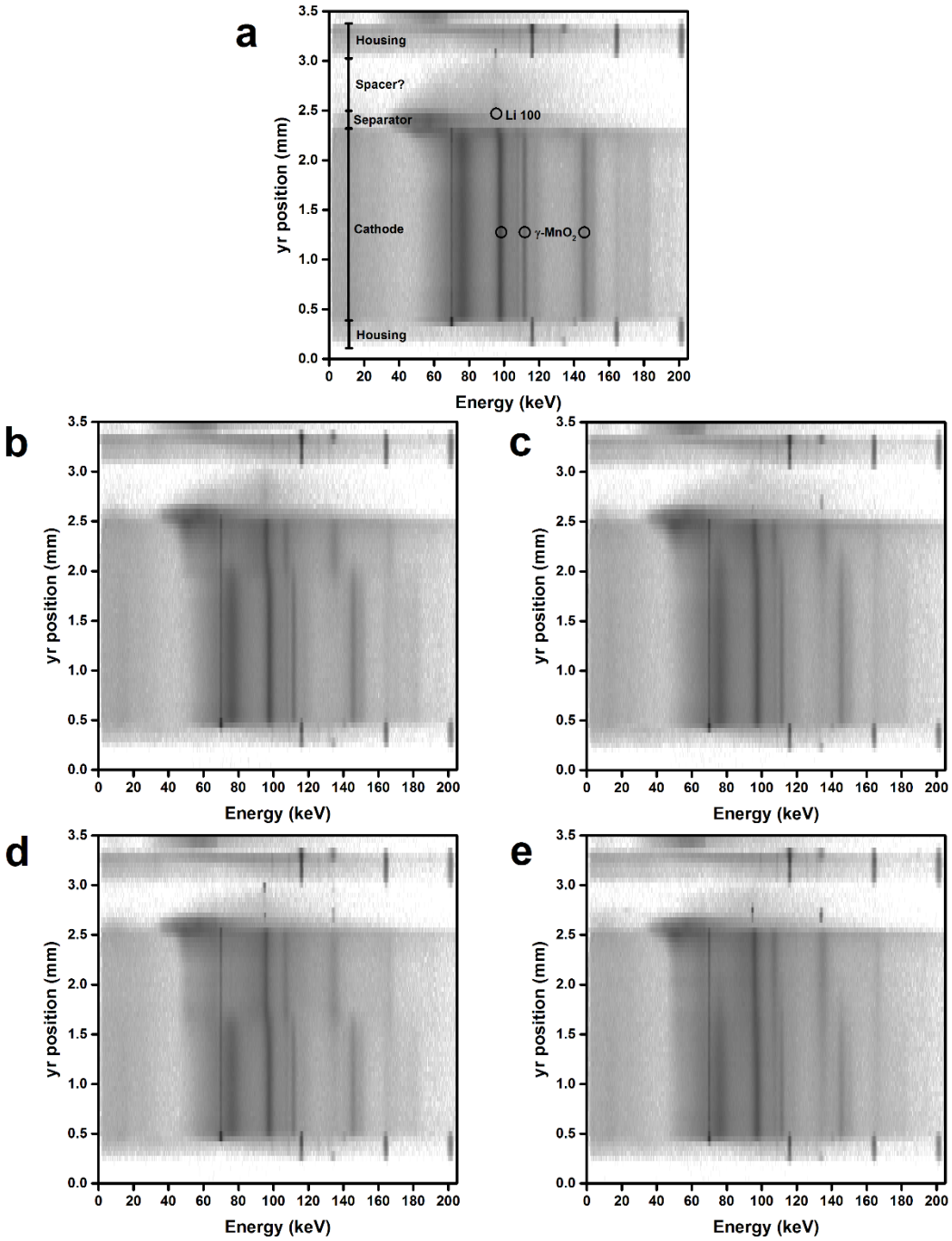

Figure 5.7 Phase maps of MnO2 (CR2032) cells

a. as-is; **b**. 20% DoD 5 mA; **c**. 20% DoD 0.5 mA; **d**. 40% DoD 5 mA; **e**. 40% DoD 0.5 mA

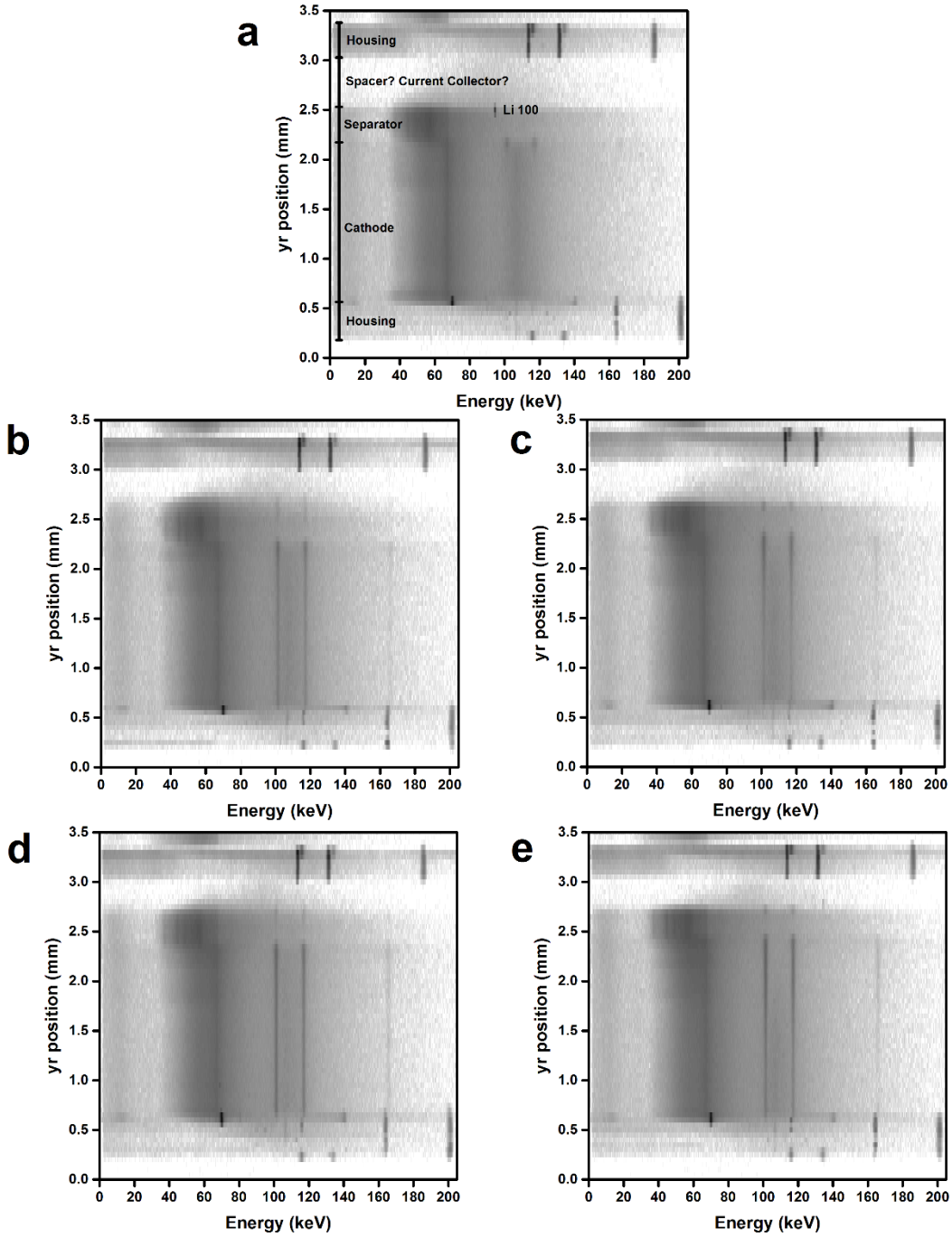

Figure 5.8 Phase maps of CFx (BR2032) cells

a. as-is; **b**. 20% DoD 2.5 mA; **c**. 20% DoD 0.25 mA; **d**. 40% DoD 2.5 mA; **e**. 40% DoD 0.25 mA

5.2.6 Further reading

[1] Rodriguez, Keenan, Nagasubramanian, Journal of Applied Crystallography. 40 (2007) 1097-1104.

[2] P. Lam, R. Yazami, Journal of Power Sources. 153 (2006) 354-359.

[3] S.S. Zhang, D. Foster, J. Wolfenstine, J. Read, Journal of Power Sources. 187 (2009) 233-237.

[4] Read, Collins, Piekarski, Zhang, Journal of The Electrochemical Society. 158 (2011) A504-A510.

[5] M. Wojdyr, Journal of Applied Crystallography. 43 (2010) 1126–1128.

6. Summary and Future Work

This dissertation has explored the use of energy dispersive synchrotron x-ray diffraction as a characterization tool for batteries. The motivation for its use was discussed. A brief technical background was given for lithium-ion batteries, x-ray diffraction, and energy-dispersive x-ray diffraction. Additionally, concerns specific to the study of lithium-ion batteries with energy dispersive x-ray diffraction are discussed.

A study of inhomogeneity in an 8 Ah high-capacity lithium iron phosphate cell was discussed. The chemical composition was estimated through a reference intensity ratio method on the $LiFePO_4$ (311) and the $FePO_4$ (020) reflections. *Operando* electrode depth profiling was achieved during discharge conditions and revealed asynchronous discharge behavior and incomplete electrode utilization. Additionally, in-plane electrode measurements were made *in-situ* while the cell was discharged. Inhomogeneous behavior was observed across nine in-plane regions and a severely delayed discharge occurred at two of the regions. The ensemble behavior is linear suggesting the importance of micro- versus macro- observations. Overall, we attribute the inhomogeneous behavior to heterogeneous conductive coating on the particles as the data follows the resistive-reactant model closely.

Additionally, *operando* energy-dispersive x-ray diffraction measurements were made on a full-sized lithium iron phosphate battery. An asynchronous response was observed in the positive electrode. Spatially and temporally resolved phase mapping was achieved at nine different time points while discharging the battery. A mole fraction phase analysis using the reference intensity ratio method was completed for the positive electrode. The results show limited diffusion towards the end of the discharge cycle as well as an asynchronous electrode utilization response. The results confirm that the asynchronous behavior is not just an artifact of

in-situ cell designs and occurs in fully-assembled batteries as well. We attribute this behavior to be a consequence of performing a local measurement over a wide-area heterogeneous reaction.

Lastly, the preliminary evidence for inhomogeneity in lithium iron phosphate is given along with depth-profiling data from both carbon monoflouride and manganese dioxide primary lithium cells.

Looking forward, there are a few areas for future work to be focused. The first is instrumentation improvement. Computer software should be continually developed to improve the capabilities and user-friendliness. Appendix A in this dissertation provides a first step towards providing a complete package of tools for analysis. It is important to note that Hui Zhong from Brookhaven and Yan Gao from General Electric Research have begun developing software for controlling experiments and visualizing data for near-real-time analysis. While this is an important endeavor, it is still prudent to have an equally full software package for more detailed analysis when away the beamline.

Along with improved software should be an improved detector system. Work has already begun towards a multi-element detector. A multi-element detector will allow for better counting statistics and less instrumental broadening. Such detector is necessary for maintaining the same level of performance while the beamline is housed at the Advanced Photon Source at Argonne National Laboratory.

Future work towards battery characterization should follow the work in Chapter 3 and attempt to observe path dependence. This can be achieved by tracking multiple areas within a cell through a series of partial discharge and charge sequences. A protocol for this procedure is given by Safari and Delacourt, (Journal of The Electrochemical Society. 158 (2011) A562-A571.).

Future work should also include additional CR and BR coin cell studies with the goal of separating transient and relaxation discharge effects. The cells should follow an analogous discharge procedure as before but directly before they are measured with EDXRD. Mapped concentration profiles should be compared with those presented in chapter five.

Regarding the technique, more work could be done on understanding the effects of the beam radiation on the samples. There is evidence to believe that the cells absorb radiation. In situ impedance spectroscopy could be carried out while a battery is irradiated by the beam as a way to provide insight in to radiation effects.

Lastly, there are many new electrochemical systems that could be better understood by the use of spatial and temporal mapping with EDXRD. I encourage the reader to involve their imagination and try something new. Indeed that is what science and experimentation is about.

Appendix A. Tools for Data Analysis

All tools (except fityk) can be downloaded at http:/www.willpaxton.com/edxrd.

A.1 CNF Converter

Data files from the X17B1 beamline prior to year 2013 are encoded in a proprietary format from Canberra. These files have a .CNF extension and are un-openable by any common software. A script was adapted in python to extract the data from the CNF files and convert them to a single column .CSV file. An additional script was written in BATCH format to automate the process of conversion for

A.2 Peak Fitting: Fityk

The program, fityk, was used extensively for the analysis of EDXRD data. It has the capability to view the files in their native *.xy format and transform the dataset from channel number to energy and to d-spacing. It is suggested to do all peak fitting in channel number or energy space.

The process of peak fitting involves the following:

- Loading of data and conversion to energy space
- Identification of the peaks present in the spectra
- Selection of the part of the spectrum to be fit (Note: whole pattern fitting is possible but it is time consuming and often not necessary.)
- Removal of background
- Initial marking of peak locations (Note: It is important to give the computer a good first estimate as to where the peaks are.)
- Check the residual difference plot for quality of fit and repeat
- Export peak parameters

The fityk software can be downloaded at http:/fityk.nieto.pl. There is an older free version and an up-to-date version which one must pay for. The most up-to-date software is recommended.

A.3 Batch Peak Fitting Script

For large data sets it is possible to automate the peak fitting process. For this purpose, a script was written in the Lua language and can be run in the fityk GUI and in the fityk command line program (cfityk.exe).

A.4 Lattice Parameter Calculator

The lattice parameter calculator was developed in MATLAB using the fsolve function. It is able to compute the lattice parameters and angles for cubic, tetragonal, orthorhombic, rhombohedral, monoclinic, triclinic, and hexagonal structures. The calculation is a non-linear least squares method employing the Levenberg-Marquardt algorithm. Calculations can be computed in a high throughput fashion by preparing a file of the following format:

```
  hkl  hkl  hkl  hkl  hkl   hkl
  eVA  eVA  eVA  eVA  eVA  eVA
1 data  data  data  data  data  data
2 data  data  data  data  data  data
...................................
n data  data  data  data  data  data
```

where the first row is the miller index of the reflection, the second row represents the unit of the data, each subsequent row is a collection of peak centers for a given spectra n.

A.5 Time Stamp Extractor

For time-resolved studies it is important to know the exact times at which each spectra was collected. When setting up an experiment, the operator choses a time interval and total number for spectra collected. However, the actual collection time is less than each time interval. Additionally, there is an additional time for computer processing and motor movement before the next spectra is collected. Therefor it is an unreasonable assumption that if you have 200

spectra collected at 30 seconds each that the total experiment time is 30x200. In fact, it is more than this.

The time stamp extractor was written to extract the exact time at which each spectra was collected. This is very useful when recording of another time-dependant variable and calibration between the two is necessary; for example, when measuring temperature, current, and/or voltage.

The time stamp extractor requires the full xy diffraction file provided at the beginning of the data set. The script runs in MATLAB and exports the time stamps in an excel file.

Appendix B. Anisotropic thermal expansion of zirconium diboride

B.1 Preface

The following is a paper intended to be submitted to a journal relevant to the field. The authors on the paper are William A. Paxton, Tevfik Ozdemir, İlyas Şavkliyildiz, Ankur U. Choksi, Terence Whalen, Zhong Zhong, and Thomas Tsakalakos. The work was completed under the grant that provided my funding.

B.2 Abstract

Zirconium diboride (ZrB_2) is an attractive material due to its thermal and electrical properties. In recent years, ZrB_2 has been investigated as a superior replacement for sapphire when used as a substrate for gallium nitride devices. Like sapphire, ZrB_2 has anisotropic hexagonal structure which defines its directionally-dependent properties. However, the anisotropic behavior of ZrB2 is not well understood. In the paper, we use energy dispersive x-ray diffraction to measure with high-precision the thermal expansion of polycrystalline zirconium diboride powder from 300 – 1150 K. Nine reflections are fit using Pseudo-Voigt peak shapes and the a and c lattice parameters are computed using a non-linear least-squares approximation. The temperature-dependent instantaneous thermal expansion coefficients are determined for each a-axis and c-axis directions and are described by the following equations:

$$\propto_a = \frac{4.1507\times10^{-6}+5.1086\times10^{-9}\,(T-293.15)}{1+4.1507\times10^{-6}(T-293.15)+2.5543\times10^{-9}\,(T-293.15)^2}$$

$$\propto_c = \frac{4.5374\times10^{-6}+4.3004\times10^{-9}\,(T-293.15)}{1+4.5374\times10^{-6}(T-293.15)+2.1502\times10^{-9}\,(T-293.15)^2}$$

Our results are within range of previously reported values but describe the temperature anisotropy in more detail. We show that anisotropic expansion coefficients converge to the same value at about 780 K and diverge at higher temperatures, an effect which has also been reported in the literature.

B.3 Introduction

Zirconium diboride (ZrB2) is a non-oxide ceramic material with a melting temperature of 3245 °C and good electrical conductivity (10^7 S/m). [1] The ultra-high melting temperature and resistance to oxidation of zirconium diboride make the material attractive for applications in ultrasonic flight, continuous steel processing, and atmospheric reentry. [1-3] Zirconium diboride is also unique, however for its electronic properties. Recently, single crystal zirconium diboride has been used as a substrate for gallium nitride (GaN) semiconductor devices. [4,5] Zirconium diboride has intrinsic advantages over sapphire which is the industry standard for GaN substrates: a smaller lattice mismatch and better electronic and thermal conductivity.

Use in any of the above applications requires a good understanding of the thermal behavior of zirconium diboride. The crystal arrangement of zirconium diboride is hexagonal with alternating layers of Zr and B atoms. [1] The hexagonal nature of ZrB2 leads to anisotropic behavior and properties which are crucial to understand in applications where the orientation of ZrB2 is controlled.

Thermal expansion has been measured in zirconium diboride in the past. The pioneering work by Kinoshita and coworkers was able to show that zirconium diboride is a viable substrate for GaN electronics. They were able to grow single crystals of ZrB2 using the RF float zone method and measure the coefficient of thermal expansion along the a direction. [4] Thermal expansion was later studied by Okamoto et al. where they similarly grew single crystals and measured expansion in both the a and c directions using a pushrod type dilatometer from room temperature to 1073 K. Their results revealed the anisotropic nature of thermal expansion with average coefficient of thermal expansion (CTE) values of 6.66×10^{-6} and 6.93×10^{-6} K^{-1} in the a and c directions respectively. They also however showed that these carry a temperature

dependence. The CTE of ZrB2 can also be calculated from first principles. Milman et al. performed an NPT molecular dynamics study and calculated values of thermal expansion that were within range of previous reports. While they mention that Okamoto's results show anisotropy and temperature dependence, they weren't able to address these features within their experimental framework.[6]

Scattering techniques such as X-ray diffraction can measure the distance between planes of atoms in a crystal. It is no surprise X-ray diffraction has been used extensively to measure thermal expansion. [7-12] Energy dispersive x-ray diffraction is particularly well-suited for measuring changes in interatomic distances. [13-15] This is because unlike the more-common angular-dispersive x-ray diffraction, EDXRD satisfies the scattering condition with polychromatic radiation at a fixed angle. This enables one to make very precise lattice parameter measurements. [8,16] Additionally, the use of an energy-discriminating detector means that the entire spectrum is collected in parallel, ideal for time-resolved measurements. [17]

In this paper we take advantage of the penetrative power of synchrotron radiation and measure the thermal expansion of polycrystalline zirconium diboride in situ up to 1100 K. Particular focus is given on the anisotropic effects of ZrB2's hexagonal lattice and the temperature dependence of thermal expansion.

B.4 Experimental

Polycrystalline zirconium diboride powder was obtained from H. C. Stark Corporation. (Grade B Hf min 0.2% 90% <6 µm) The powder was loosely packed in an alumina vessel and a type K thermocouple was placed in the center of the powder. The vessel was then placed in a furnace for built for high temperature in-situ diffraction work. The details of the furnace have been covered previously in the literature.[16]

Energy dispersive x-ray diffraction (EDXRD) was used at the National Synchrotron Light Source X17B1 beamline at Brookhaven National Laboratory. EDXRD uses a fixed angle for diffraction and polychromatic radiation in order to satisfy the diffraction condition. As a result, one measures directly in reciprocal space and can determine the lattice parameter with great precision. The measurement volume is fixed in space and the spectra is collected in a parallel fashion. These factors of EDXRD make it a viable technique for in-situ measurement of thermal expansion. Figure B.1 shows the experimental configuration.

The sample was heated from room temperature to about 800 °C at a heating rate of 5 ° per minute in an Ar environment to prevent oxidation. Throughout the experiment, spectra were collected every 30 seconds. Additionally, the temperature was logged by the thermocouple every one second. The clocks on both the temperature logger and the EDXRD computer were synchronized so that the temperature and EDXRD data could be correlated.

Standards for calibration were collected from Ag, Au, CeO_2, Cu, Ge, LaB_6, W, and Y_2O_3 and used to determine the channel number to energy relationship and the exact angle of diffraction.

The 001, 100, 101, 002, 110, 102, 111, 200, and 201 peaks were identified in the spectra and were fit with Pseudo-Voigt peak-shape function. [18] The d-spacing for the nine peaks present were then were then used to calculate the a and c lattice parameters using a non-linear least squares determination incorporating the Levenberg-Marquardt algorithm.

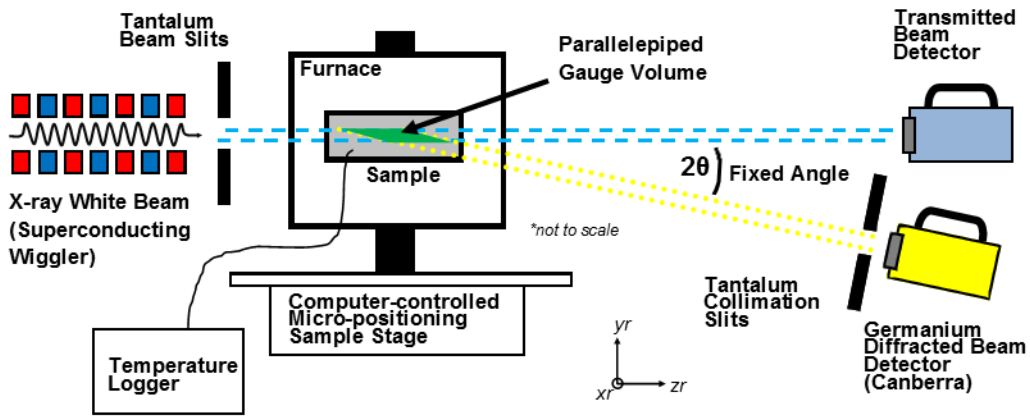

Figure B.1 Schematic of the EDXRD experiment

B.5 Results and Discussion

Figure B.2 shows the lattice parameter a as a function of temperature and Figure B.3 shows the lattice parameter c as a function of temperature. Overall, the data show a minimal degree of scatter which is should be considered a representation of the error in both the peak fitting and the temperature recording. Additionally, throughout the experiment we observe a uniform thermal expansion and no structural changes.

The coefficient of thermal expansion can be written as

$$\propto = \frac{1}{l}\frac{dl}{dT}$$

where l is a length, and $dldT$ is the rate of change of that length with temperature. Rearranging gives us

$$\frac{\Delta l}{l} = \propto \Delta T$$

The above equation assumes that the expansion coefficient does not change with temperature. For small changes in temperature, this provides a good approximation. However, the data at hand provides lattice parameters from $300\ K$ up to $1150\ K$, rendering the above approximation

useless. Let us consider the behavior of the lattice parameter over the given range of temperatures is approximated using the following second order polynomial equation

$$a(T) = a_o + \propto' (T - \Theta) + \propto'' (T - \Theta)^2$$

where a is the lattice parameter, T is the measured temperature, Θ is a reference temperature, a_o is the lattice parameter at the reference temperature, and $\propto'$ and $\propto''$ are the first and second order expansion coefficients respectively.

The lattice parameter data in both Figure B.2 and Figure B.3 are fit with the second order polynomial equation with a reference temperature of $293.15\ K$. The fitting results are given in Table B.1. Overall the fit is excellent with a coefficient of determination of 0.99826 for lattice parameter a and 0.99857 lattice parameter c.

Table B.1 Constants solved using the polynomial fit of lattice parameter versus temperature

Lattice parameter	a_o Å	$\propto'$ K^{-1}	$\propto'$ K^{-2}
a	3.14187(6)	1.304(25) x 10^{-5}	8.03(24) x 10^{-9}
c	3.49888(6)	1.587(25) x 10^{-5}	7.52(24) x 10^{-9}

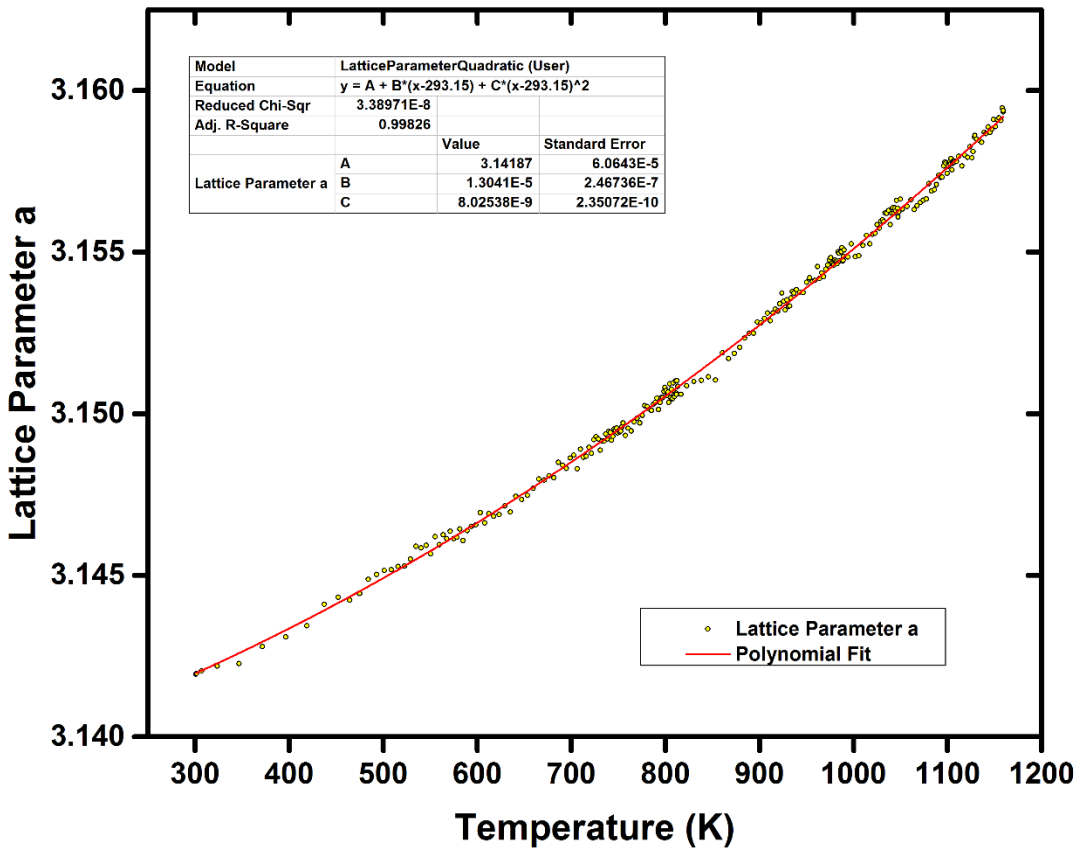

Figure B.2 Lattice constant a as a function of temperature

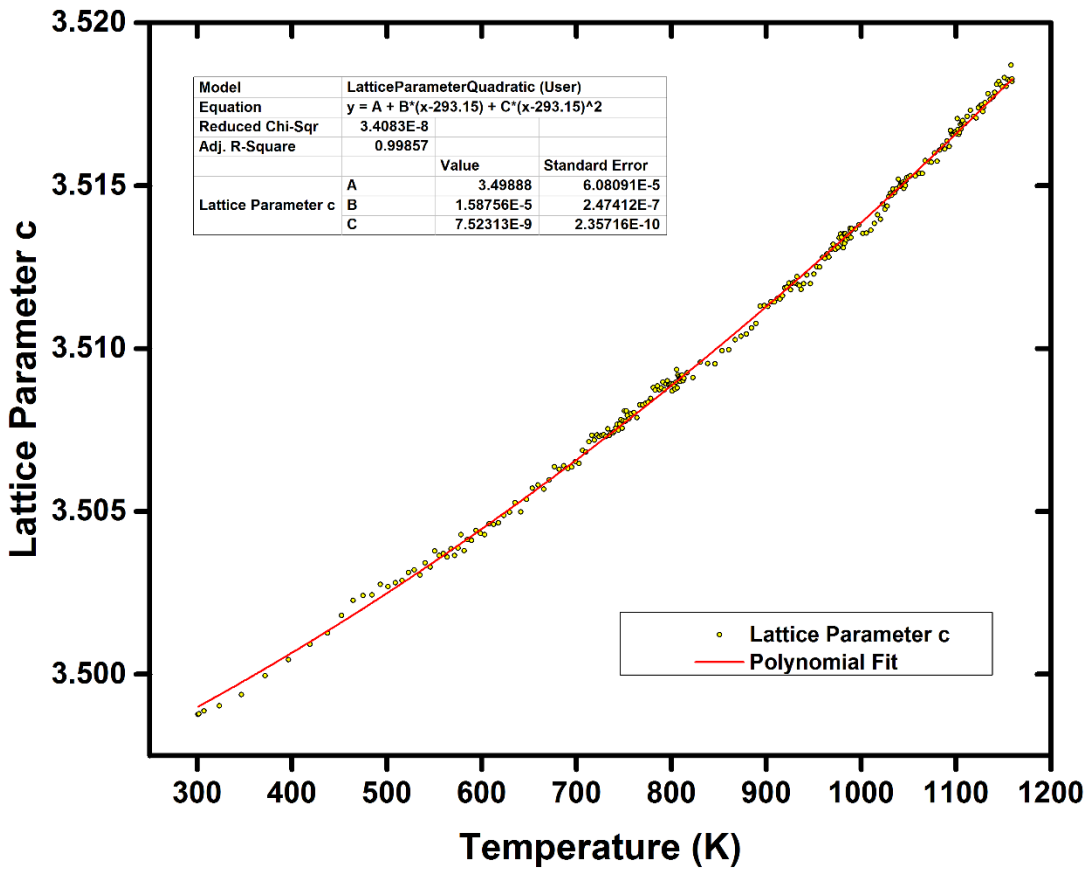

Figure B.3 Lattice constant c as a function of temperature

The quadratic behavior of the lattice parameter with temperature indicates that the coefficient of thermal expansion is linearly dependent with temperature. By taking the derivative of the fit equation and dividing by the lattice parameter, one can calculate the temperature-dependent instantaneous expansion coefficient. [19,20] This is shown in the following equation:

$$CTE = \propto (T) = \frac{\propto' + 2 \propto'' (T - \Theta)}{a_o + \propto' (T - \Theta) + \propto'' (T - \Theta)^2}$$

The CTE dependence on temperature for both the a and c lattice parameters are shown in Figure B.4. Additionally, selected values are given in Table B.2. At room temperature, we observe anisotropic behavior with the expansion larger in the c direction. The two lines converge around $780\ K$ however, at which point the CTE is isotropic. At temperatures great than $780\ K$ we observe a higher expansion in the a direction. The calculated expression for the temperature-dependent instantaneous expansion coefficient are given below:

$$\propto_a = \frac{4.1507 \times 10^{-6} + 5.1086 \times 10^{-9}\ (T - 293.15)}{1 + 4.1507 \times 10^{-6}(T - 293.15) + 2.5543 \times 10^{-9}\ (T - 293.15)^2}$$

$$\propto_c = \frac{4.5374 \times 10^{-6} + 4.3004 \times 10^{-9}\ (T - 293.15)}{1 + 4.5374 \times 10^{-6}(T - 293.15) + 2.1502 \times 10^{-9}\ (T - 293.15)^2}$$

There are some interesting differences when comparing our results with other values reported in the literature with our results. CTE values from Okamoto *et al.* and Milman *et al.* are plotted on Figure 4 at the upper limit of the temperature range reported. Above 650 K there is good agreement between our values and those reported by others. However, below 650 K our values are significantly lower than that of Okamoto *et al.*. Because this is within operating temperature range of a typical GaN LED, it is important to understand the results. It is well known for thermal expansion that lattice parameter measurements differ from macroscopic measurements. Particularly, our diffraction is not sensitive to the increases in thermodynamic defects associated with higher temperatures. Additionally, Okamoto et al. do not mention anything towards the quality of their crystal i.e. whether or not there is significant twinning or other defects. These things could explain the significantly higher values they observe.

We feel that it is important to also comment of the raw values of our computed lattice parameters. Our values are about 0.02 Angstroms lower than what we would expect from the

commercial powder. In order to confirm that there was nothing wrong with the powder, powder x-ray diffraction measurements were carried out on our laboratory diffractometer. Figure 5 shows both the EDXRD and ADXRD measurements at room temperature. We see a good agreement between the two methods and observe no secondary phases. Whole pattern fitting was carried out on the ADXRD measurement and the lattice parameters were found to be within range of the literature values. We attribute the difference in values an indication of the accuracy and precision of the EDXRD technique. Because one relies on a calibration using standards to convert from a channel number to energy and d-spacing in EDXRD, there is room for systematic error. However, because the measurements are made at a fixed angle, they are very precise. For the purpose of this experiment, we are concerned not with the actual values but how they differ with temperature. In this case, the high precision of EDXRD serves us well.

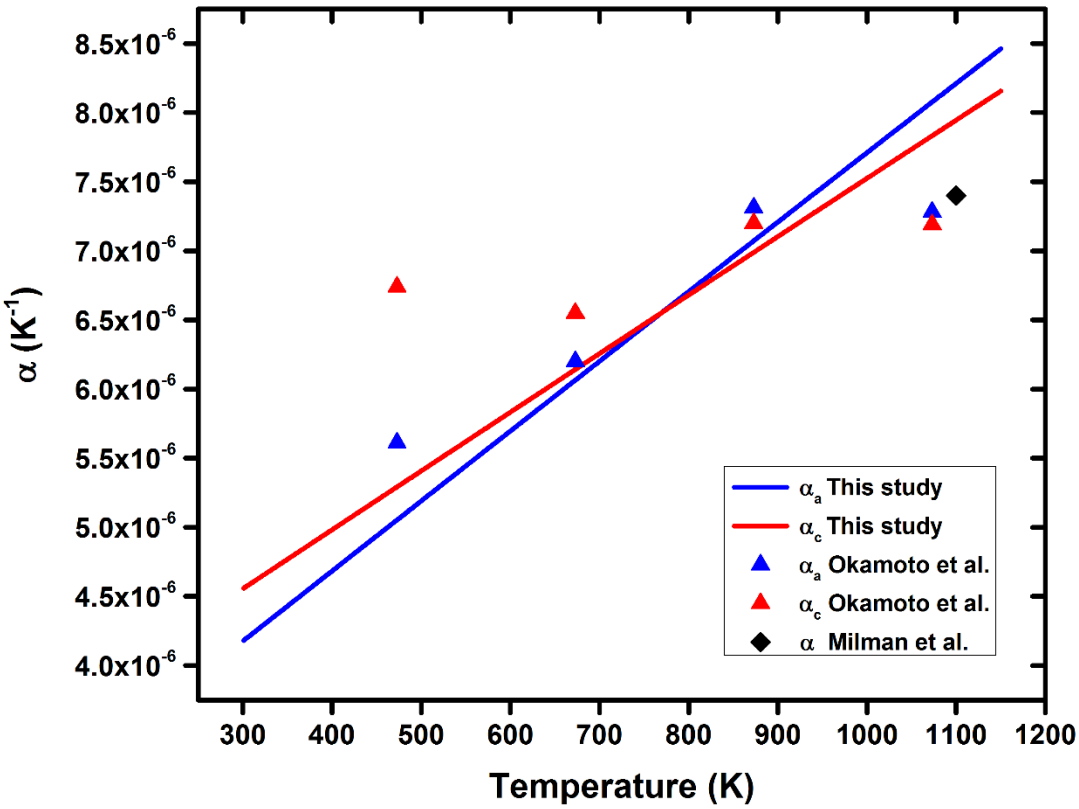

Figure B.4 Temperature dependence of coefficient of thermal expansion

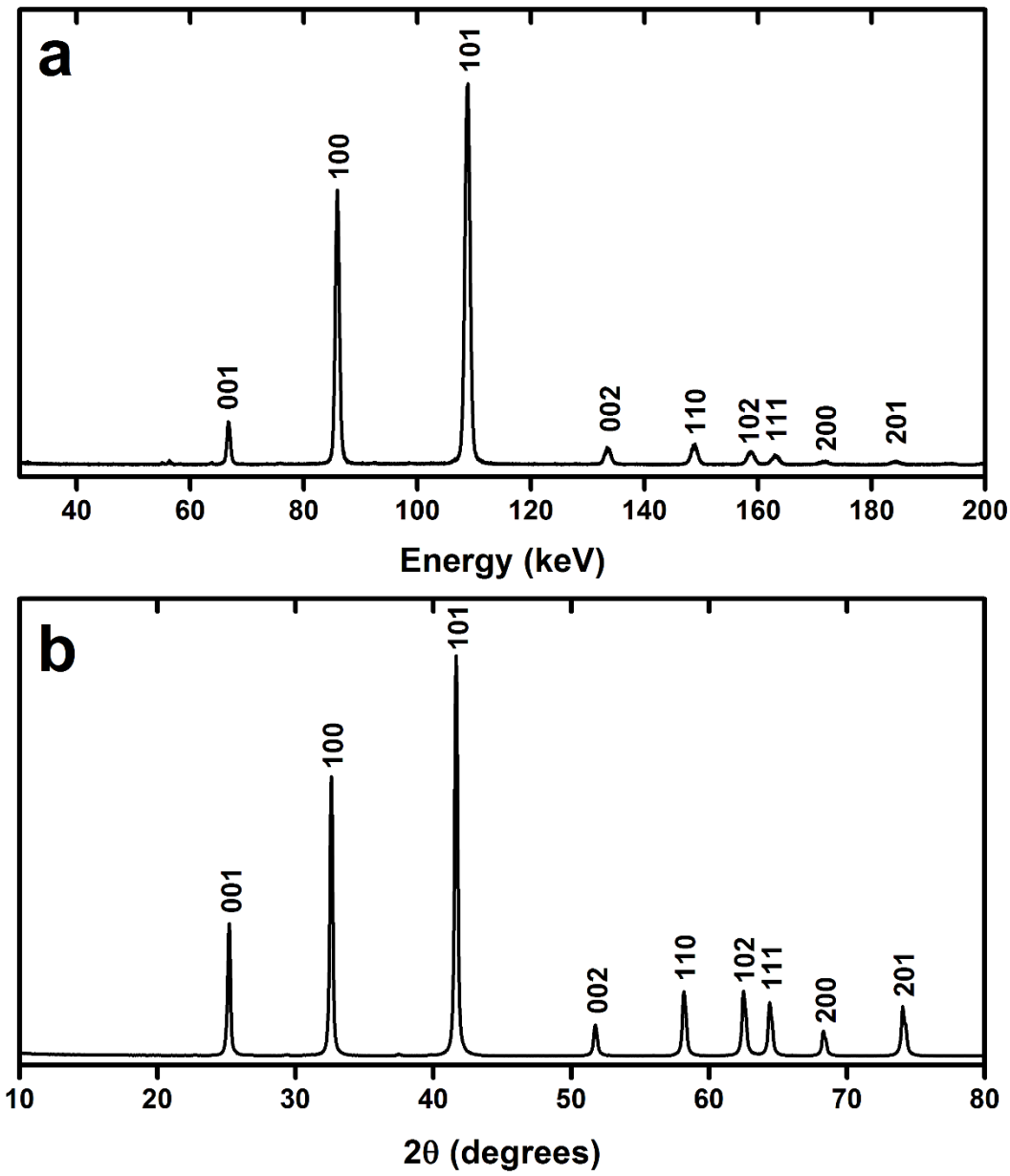

Figure B.5 Diffraction spectra

a. energy-dispersive x-ray diffraction data at 300K

b. angular-dispersive x-ray diffraction data at 300K

B.6 Conclusions

We performed energy dispersive x-ray diffraction measurements while heating a polycrystalline zirconium diboride powder from 300 to 1150 K. The temperature-dependent instantaneous thermal expansion coefficients were determined for the a-axis and c-axis directions. The results show that $\propto_a$and $\propto_c$ converge to the same value at around 780 K, below which the $\propto_c$ is higher and above which the $\propto_a$ is higher.

Table B.2 Instantaneous values of expansion coefficient at selected temperatures

Temperature K	$\propto_a$ x 10^{-6} K^{-1}	$\propto_c$ x 10^{-6} K^{-1}
300	4.17	4.55
400	4.68	4.98
500	5.19	5.41
600	5.70	5.83
700	6.20	6.26
800	6.71	6.68
900	7.21	7.10
1000	7.71	7.52
1100	8.21	7.95

B.7 Acknowledgements

The authors acknowledge Bart Visser, Hülya Biçer, and Dr. E. Koray Akdoğan for their support in the laboratory and helpful discussions. This research was supported by the Office of Naval Research Grant Number N00014-13-1-0164 entitled Thermokinetic Origins of Sintering in Nanocrystalline Ceramics by In-Situ High Temperature and Pressure Synchrotron Energy Dispersive X-ray Diffraction.

B.8 References

[1] Fahrenholtz WG, Hilmas GE, Talmy IG, Zaykoski JA, Journal of the American Ceramic Society, 90 (2007) 1347–1364.

[2] Chamberlain AL, Fahrenholtz WG, Hilmas GE, Ellerby DT, Journal of the American Ceramic Society, 87 (2004) 1170–1172.

[3] Chamberlain AL, Fahrenholtz WG, Hilmas GE, Journal of the American Ceramic Society, 89 (2006) 450–456.

[4] Kinoshita, Otani, Kamiyama, et al., Japanese Journal of Applied Physics, 40 (2001) L1280-L1282.

[5] Kinoshita, Otani, Kamiyama, et al., Japanese Journal of Applied Physics, 42 (2003) 2260-2264.

[6] Milman, Winkler, Probert, Journal of Physics: Condensed Matter, 17 (2005) 2233-2241.

[7] Edwards, Speiser, Johnston, Journal of Applied Physics, 22 (1951) 424.

[8] Buras, Olsen, Gerward, Will, Hinze, Journal of Applied Crystallography, 10 (1977) 431-438.

[9] Mary, Evans, Vogt, Sleight, Science, 272 (1996) 90-92.

[10] Chin, Schoenlein, Glover, Balling, Leemans, Shank, Physical Review Letters, 83 (1999) 336-339.

[11] Udachin, Ratcliffe, Ripmeester, The Journal of Physical Chemistry B, 105 (2001) 4204.

[12] Maniwa, Fujiwara, Kira, et al., Physical Review B., 64 (2001).

[13] Croft, Zakharchenko, Zhong, et al., Journal of Applied Physics, 92 (2002) 578.

[14] Croft M, Zhong Z, Jisrawi N, et al., International Journal of Fatigue, 27 (2005) 1408-1419.

[15] Rijssenbeek J, Gao Y, Zhong Z, et al., Journal of Power Sources, 196 (2011) 2332-2339.

[16] Akdoğan, Şavklıyıldız, Biçer, et al., Journal of Applied Physics, 113 (2013) 233503.

[17] Kämpfe B, Luczak F, Michel B., Particle & Particle Systems Characterization, 22 (2005) 391–396.

[18] Wojdyr M., Journal of Applied Crystallography, 43 (2010) 1126–1128.

[19] Harris D. Materials for infrared windows and domes: Properties and performance (SPIE press monograph vol. PM70). Society of Photo Optical; (1999).

[20] Bagdade S, ASM. ASM ready reference: Thermal properties of metals (materials data series). ASM International; (2002).